

# Transformable multirotor with two-dimensional multilinks: Modeling, control, and whole-body aerial manipulation

Moju Zhao, Koji Kawasaki, Tomoki Anzai, Xiangyu Chen, Shintaro Noda,  
Fan Shi, Kei Okada and Masayuki Inaba

## Abstract

A multirotor with two-dimensional multilinks is proposed to perform aerial transformation and aerial manipulation. First, a modular link structure that comprises a multirotor with a reliable internal communication system was initially developed. Second, a flight control method was further introduced on the basis of linear-quadratic-integral optimal control for aerial transformation. A relaxed hovering solution that neglects the yaw motion stability is proposed to enable stable flight under a certain singular form. Third, the transformable robot was employed as an entire gripper with regards to grasping to perform the whole-body aerial manipulation. A grasp-form searching method was developed to optimize hovering thrust force and joint torque under force-closure grasp, and was followed by an aerial approach and grasp-motion strategy to fulfill the resulting desired grasp form. Finally, experimental results demonstrate the stable aerial transformation as well as the feasibility of the whole-body aerial manipulation system to grasp and carry different types of objects.

## Keywords

transformable multirotor, modeling and control, aerial manipulation

## 1. Introduction

Multirotors have been used and investigated extensively because of their high mobility in three-dimensional environments (Kumar and Michael, 2012; Mahony et al., 2012) and in various fields such as disaster response (Michael et al., 2012), inspection (Kawasaki et al., 2015), and surveillance (Doitsidis et al., 2012). Their ability to perform tasks that influence their environment is also of considerable interest; one such representative motion is the use of aerial manipulation to grasp and carry objects (Lindsey et al., 2012).

Several types of end effectors for aerial grasping have been developed and can be classified into two types: those using mechanical force-closure (Backus et al., 2014; Lippiello et al., 2016; Pounds et al., 2011) and those using suction force (Anzai et al., 2017; CHO and SHIM, 2017; Gawel et al., 2017). As an exception, Mellinger et al. (2011) employed hooks to perform grasping with possible penetration on the object surface. Using force-closure can provide stable grasping; however, it is difficult to grasp any object that is larger than the gripper. On the other hand, suction power, generated by either magnetic force or negative pressure, only requires a small surface to impose the force

and can lift relatively large object. Regardless, because the majority of mechanisms are attached to the bottom of the aerial robot and because the object hangs under the multirotor, the downwash flow poses a big challenge.

Drawing inspiration from the enveloping grasp that is made possible by planar whole-arm manipulation (Seo et al., 2012), an aerial robot with two-dimensional multilinks is proposed to achieve whole-body aerial manipulation using the edges of propeller ducts, as depicted in Figure 1. As the rotor is embedded inside the link module, the target object is not influenced by the downwash flow, because the object and rotors are located at a similar height. Furthermore, an aerial robot comprising large number of links would allow large objects to be grasped. This research only considers situations in which the multilinked aerial robot can completely enclose the object. In addition, the target object is

---

Department of Mechano-Informatics, The University of Tokyo, Tokyo, Japan

### Corresponding author:

Moju Zhao, Department of Mechano-Informatics, The University of Tokyo, 7-3-1 Hongo, Bunkyo-ku, Tokyo 113-8656, Japan.  
Email: chou@jsk.imi.i.u-tokyo.ac.jp

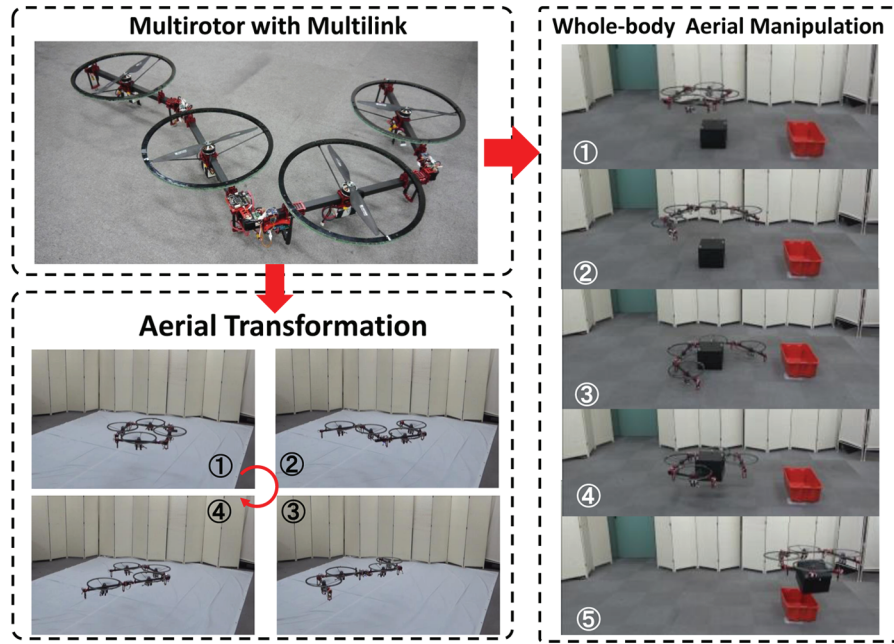


**Fig. 1.** The developed multirotor with two-dimensional multilinks that is capable of aerial transformation and whole-body aerial manipulation. The propeller is embedded inside the link module and is enclosed by the duct.

assumed to be regular (a cylinder or a convex polygonal column) with uniform density, which ensures that it is easy to calculate the object's center of gravity (CoG).

### 1.1. Related work

A multirotor with two-dimensional multilinks involves an arbitrary configured  $N$ -rotor system. Oung and D'Andrea (2014) initially presented a modeling method for this system and achieved a modular and assemblable aerial robot without joints (thus, no kinematics change). Because internal communication presents a challenge for this generalized system, a peer communication system was constructed between the neighboring link modules by Oung and D'Andrea (2014). However, multilinked kinematics requires the existence of master-slave relations to communicate all the statuses to the master node (e.g., joint angles). Previously, a star topology that connects the flight controller board with each component (i.e., a joint module and rotor speed controller) was applied in our previous work (Zhao et al., 2016). However, this topology is not adaptive for  $N$ -rotor systems because the number of communication cables and I/O ports increases proportionally as the number of links increases. Therefore, a reliable internal communication system based on a single shared bus and a highly modulized link structure is required. Although development of such a system is likely to increase the complexity of the mechanical and electrical design, it is the optimal solution to the aerial transformation to the best of our knowledge.

Regarding to the flight control for a reconfigurable  $N$ -rotor system, Oung et al. (2009) first proposed a method that was assumed to be relatively circular. Mellinger et al.

(2013) presented a similar control framework in which the multiple quadrotors were applied to cooperatively manipulate a rigidly attached object. Unlike these static  $N$ -rotor configurations, real-time optimal control systems, which update the feedback control gains according to the kinematics of multilinks, was proposed in our previous work (Zhao et al., 2016). In this previous work, the transformation is assumed to be slow, thus the multilinked dynamics was described as a single rigid body with variant inertial parameters. However, it was not possible to fly under such singular forms that the proposed control method could not stabilize the full states (i.e., attitude and altitude). Alternatively, Mueller and D'Andrea (2016) presented a relaxed definition of hovering for multirotors and a control methodology allowing for stabilization with only one propeller (i.e., failure of three propellers in quadrotor model) under this relaxed hovering condition. In our work, a similar relaxed hovering solution that neglects yaw stability is observed under a certain type of singular form; further, an associated control method that focuses on translational stability is developed.

The force-closure grasp by the whole-arm manipulation has been analyzed by Watanabe et al. (2006). Regarding aerial grasping, Backus et al. (2014) developed a vertical gripper that takes friction into account under a force-closure situation. In contrast, our study focuses on the manipulation by a horizontal gripper using the edges of the ducts, where the influence of gravity direction is different. In our previous work (Zhao et al., 2017), the grasp-form searching method was developed to find a grasp form that minimizes the norm of the joint torque. Nevertheless, the change in inertial parameters after grasping was not considered,

implying the possibility of unstable flight as discussed by Mellinger et al. (2011). Therefore, an improved cost function that adds the consideration on the change of hovering thrust forces is designed in the proposed searching method. The approach and grasp motion strategy is another important issue; further, the disturbance that is caused by the floor and the object while approaching and grasping poses a big challenge. The passively adaptive grasping motion that was proposed in our previous work (Zhao et al., 2017) reduced the influence of such disturbance. However, it was highly dependent on the slipping motion between the propeller duct and object, implying the stuck problem when joint torque could not overcome the static friction on the surface. Therefore, an improved motion strategy is proposed in this paper to overcome the static friction.

This study builds on our previous work (Zhao et al., 2017, 2016) and extends the results by:

- developing a reliable internal communication system comprising a shared bus and modulized links;
- analyzing a relaxed hovering solution for a certain singular form, defined as the semi-stabilizable form, and developing the related flight control to achieve translational stability;
- improving the grasp-form searching method by considering the variation of hovering thrust (propeller) forces during the grasp-form searching, and determining the optimal range of valid grasp forms rather than a single form to ensure robustness against the model error and sensing noise in the real situation;
- improving the approach and grasp motion strategy to minimize the influence of disturbances from the floor and object and guarantee the reach of desired grasping form resulting from proposed searching method, by taking advantage of the relative motion on an object surface (i.e., rolling motion with friction and sliding without friction).

### 1.2. Notation

All the symbols in this paper are explained at their first appearance. Boldface symbols (e.g.,  $\mathbf{r}$ ) denote vectors, whereas non-boldface symbols (e.g.,  $m$  or  $I$ ) are used to denote scalars or matrices. The coordinate system in which a vector is expressed is denoted by a superscript, e.g.,  ${}^{(W)}\mathbf{r}$  expresses  $\mathbf{r}$  with reference to the frame  $\{W\}$ . Subscripts are used to express a relation or attribute, e.g.,  ${}^{(W)}r_{x_{des}}$  represents the desired value of position on the  $x$  axis with reference to the frame  $\{W\}$ . For convenience, the vector,  $\boldsymbol{\alpha}$ , is used to represent the Euler angles (roll, pitch, yaw).

### 1.3. Organization

This paper is divided into three parts. The first part begins with Section 2, where an internal communication system based on the shared bus and the quadrotor prototype are explained in detail; further, in Section 3, the dynamic model

and flight control for aerial transformation are derived. In addition, the singular forms and relaxed hovering solution are presented. The second part begins with Section 4, where a searching method to find the optimal grasp form based on the force-closure along with the hovering thrust forces is proposed. Subsequently, the motion strategy regarding to the aerial approaching and grasping is described in Section 5. Finally, the experimental results are presented in Section 6, and the feasibility of aerial transformation and the whole-body aerial manipulation for grasping and carrying the cylindrical and box-type objects is demonstrated.

## 2. System description

### 2.1. Multilinked structure

The transformable multirotor comprises link modules with embedded propellers and joint modules actuated by the servo motors as depicted in Figure 2. All the joints exhibit parallel axes of rotation, resulting in two-dimensional transformation. The propeller spins in the opposite direction as that of the neighboring rotors; further, the propeller duct plays an important role in terms of aerial manipulation and the protection.

### 2.2. Internal communication system based on a shared bus

As mentioned in Section 1, a generalized communication system is indispensable for the  $N$ -rotor configuration system. The inter-module communication network developed by Oung and D'Andrea (2014) only allowed the inertial measurement unit (IMU) information to be exchanged between neighboring link modules. This is not suitable for multilinked structures, because all the joint angles should be gathered to a master node to update the kinematics, which is necessary for the flight control. Furthermore, the desired propeller speeds and joint angles must be

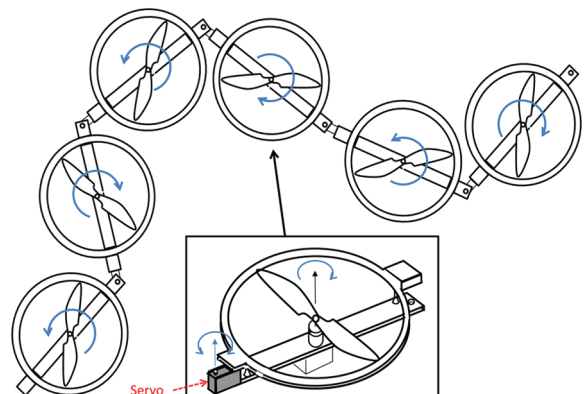


**Fig. 2.** Example of multilinked structure comprising six link modules. Each link module contains a propeller rotor with a thin duct and a servo module at each end. A battery is distributed at each link.

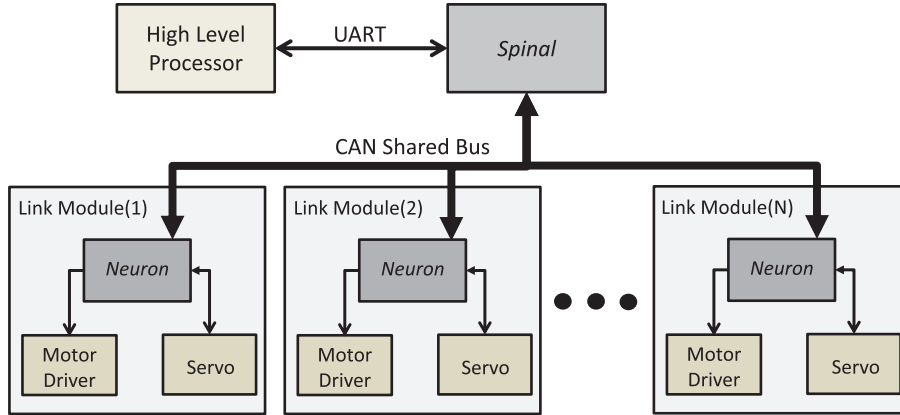


**Fig. 3.** The internal communication system based on the CAN protocol. The main controller board module is called *Spinal*, whereas the sub-controller board module is called *Neuron*.

transmitted from the master node to each propeller rotor and joint module, respectively. A simple start topology can be applied in the case of a small number of links (e.g.,  $N = 4$ ); however, this is not suitable for a reconfigurable  $N$ -rotor system owing to an increase in the number of communication cables and I/O ports. Hence, a shared bus is introduced for a multilinked aerial robot.

An internal communication system with a shared bus is commonly used for general multilinked robots such as humanoids (Kojima et al., 2015; Urata et al., 2010). However, the majority of communication systems for these robots are accompanied by heavy devices, which are a burden to the flight payload. Thus, in our work, the controller area network (CAN) that was introduced by ISO (1993) is applied, because of its high reliability, good real-time performance, and low cost. As shown in Figure 3, the main system controller board called *Spinal* and the sub-controller board in each link module called *Neuron* that collects data from each basic device are connected by the shared bus. In addition, the high-level processor that is responsible for heavy processes is connected to *Spinal* by point-to-point communication. *Spinal* is expected to be located at the center of the multilinked structure to ensure symmetry with respect to the communication layer.

### 2.3. Link module

A link module is further designed to contain a *Neuron* that is directly connected to the joint servo module and motor driver, as shown in Figure 4. The main specifications of each link module are presented in Table 1. A propeller duct with an aluminum honeycomb structure is employed as the gripper surface for whole-body manipulation. Because the battery is distributed at each link, the flight time should remain constant regardless of the number of links if no additional payload is added. The power is shared by all link modules to guarantee the same voltage level for each rotor.

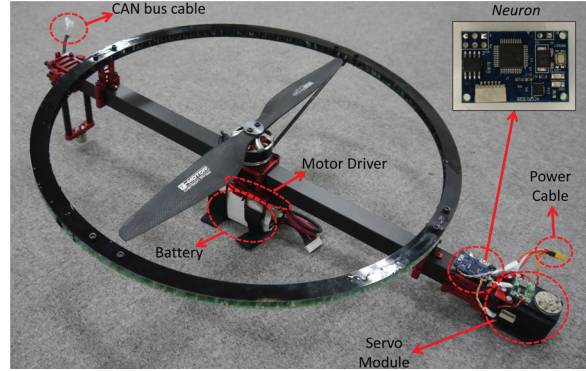


**Fig. 4.** Link module structure.

**Table 1.** Link module specifications.

Symbol	Description	Value
$l_L$	Link length (m)	0.6
$R_{duct}$	Propeller duct radius (m)	0.2
$m_{link}$	Mass (kg)	0.8
-	motor (Kv)	360
-	propeller (in.)	14
-	battery voltage (V)	22.2
-	battery capacity (mAh)	1,300
-	flight time (min)	15
-	<i>Neuron</i>	STM32F1
-	joint servo motor	Dynamixel MX28AR

This is achieved by the shared power bus as shown in Figure 4.

### 2.4. Quadrotor prototype with four links

Using link modules described above, the prototype composed of four links and three joints is constructed as shown in Figure 5 and Table 2. Two-dimensional transformation is



**Fig. 5.** Quad-rotor prototype composed of four link modules with the proposed internal communication system.

**Table 2.** Prototype specifications.

Symbol	Description	Value
$M$	Total mass (kg)	3.34
-	<i>Spinal</i>	STM32F7
$m_{spinal}$	Mass of <i>Spinal</i> (kg)	0.04
-	High-level processor	Odroid XU4
$m_{hl\ processor}$	Mass of high-level processor (kg)	0.1

achieved within the rotation range  $-\frac{\pi}{2}$  rad to  $\frac{\pi}{2}$  rad at each joint. The total weight of the prototype is 3.34 kg.

### 3. Control for aerial transformation

#### 3.1. Dynamic model of multilinks

We assume that the multilinks act as a single rigid body at each time point, because aerial transformation is performed slowly. With this assumption, we can perform forward kinematics with the joint angles  $\boldsymbol{\theta}$  as proposed by Zhao et al. (2016). As shown in Figure 6, the goal of the forward kinematics in this work is to calculate the relative position and orientation of the  $\{CoG\}$  frame, and express the dynamics of multilinks in the  $\{CoG\}$  frame. Forward kinematics generally start from the root of the multilinked structure (i.e., the end of the link rod). However, the start position is selected as where the main controller board *Spinal* is located for convenience. The corresponding link to this start position is defined as the baselink; further, the orientation of the baselink is identical to the  $\{CoG\}$  frame. In the quadrotor prototype (Figure 5), *Spinal* is attached at the third link (i.e., baselink) and estimates the attitude using the embedded IMU unit. Thus, the estimated attitude of *Spinal* can directly denote the attitude of the  $\{CoG\}$  frame. We define  $\{CoG\}\mathbf{r}_i = [\{CoG\}r_{x_i}, \{CoG\}r_{y_i}]^T$  as the position of the  $i$ th rotor with reference to the  $\{CoG\}$  frame. The inertia tensor  $\{CoG\}I$  expressed in the  $\{CoG\}$  frame can also be obtained according to the forward kinematics and parallel axis theorem, and varies as the joint angles change.

The lifting force and drag torque generated by the rotation of the propeller are denoted by  $F_{T_i}$  and  $M_{T_i}$ ,

respectively. According to the standard motor model, a linear relationship exists between them:

$$M_{T_i} = c_i F_{T_i}; \quad c_i = (-1)^i c \quad (1)$$

Thus, odd-numbered propellers rotate clockwise (CW), and even-numbered propellers rotate counter-clockwise (CCW).

The dynamics of the translational motion and rotational motion can then be written as follows:

$$M^{(w)}\ddot{\mathbf{r}} = {}^{(w)}R_{\{CoG\}} \begin{bmatrix} 0 \\ 0 \\ \sum_{i=1}^N F_{T_i} \end{bmatrix} + \begin{bmatrix} 0 \\ 0 \\ -Mg \end{bmatrix} \quad (2)$$

$$\{CoG\}I^{\{CoG\}}\dot{\mathbf{w}} = \begin{bmatrix} \sum_{i=1}^N \{CoG\}r_{y_i} F_{T_i} \\ -\sum_{i=1}^N \{CoG\}r_{x_i} F_{T_i} \\ \sum_{i=1}^N c_i F_{T_i} \end{bmatrix} - {}^{(w)}\mathbf{w} \times {}^{(CoG)}I^{\{CoG\}}\mathbf{w} \quad (3)$$

where  ${}^{(w)}\mathbf{r}$  is the position of the  $\{CoG\}$  frame expressed in the world frame, and  ${}^{(CoG)}\mathbf{w} = [{}^{(CoG)}w_x \ {}^{(CoG)}w_y \ {}^{(CoG)}w_z]^T$  is the angular velocity vector of the multilink expressed in the  $\{CoG\}$  frame.

We then apply the Euler angles  ${}^{(w)}\boldsymbol{\alpha}$  to present the orientation of the  $\{CoG\}$  frame with reference to the world frame. The time derivatives of Euler angles then have the following relationship with angular velocity expressed in the  $\{CoG\}$  frame:

$$\{CoG\}\dot{\mathbf{w}} = \begin{bmatrix} 1 & 0 & -\sin({}^{(w)}\alpha_y) \\ 0 & \cos({}^{(w)}\alpha_x) & \cos({}^{(w)}\alpha_y) \sin({}^{(w)}\alpha_x) \\ 0 & -\sin({}^{(w)}\alpha_x) & \cos({}^{(w)}\alpha_y) \cos({}^{(w)}\alpha_x) \end{bmatrix} {}^{(w)}\dot{\boldsymbol{\alpha}} \quad (4)$$

**3.1.1 Linearization around the hover state.** In this work, the multilink is regarded as a special rigid body of which the inertia tensor and rotor configuration vary during transformation. With this assumption, we develop a control method based on the dynamic model presented in Equations (2) and (3). The goal of flight control is to keep the body close to the hovering state, where the roll  ${}^{(w)}\alpha_x$  and pitch  ${}^{(w)}\alpha_y$  angles are small. An approximation equation while flying close to the hover state is given in

$${}^{(w)}\alpha_x \approx 0; \quad {}^{(w)}\alpha_y \approx 0 \quad (5)$$

using an approach similar to that described by Michael et al. (2010). Substituting Equation (5) into Equation (4) yields the approximation of the angular velocity in

$${}^{(w)}\dot{\boldsymbol{\alpha}} \approx {}^{(CoG)}\mathbf{w} \quad (6)$$

Subsequently, the translational motion (Equation (2)) and rotational motion (Equation (3)) can be derived as follows:

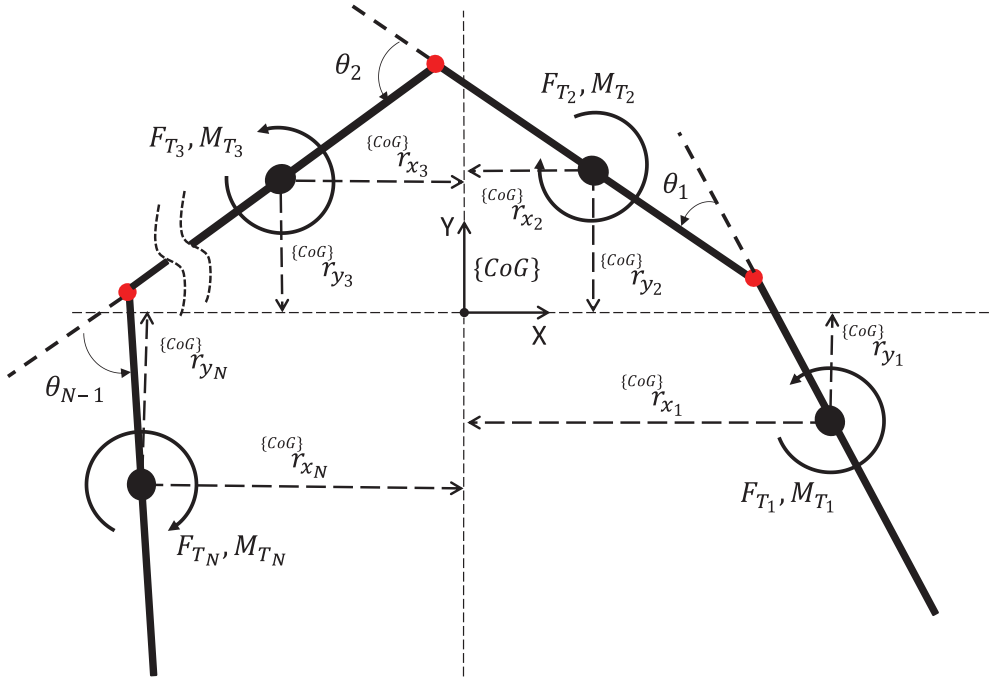


**Fig. 6.** Dynamic model of the proposed multilinked multirotor described in the  $\{\text{CoG}\}$  frame, where  $F_{T_i}$  and  $M_{T_i}$  denote the lifting force and drag torque generated by the rotation of propeller, respectively.

$$\{^{(w)}\ddot{r}_x = g(\{^{(w)}\alpha_y \cos(\{^{(w)}\alpha_z) + \{^{(w)}\alpha_x \sin(\{^{(w)}\alpha_z)) \quad (7)$$

$$\{^{(w)}\ddot{r}_y = g(\{^{(w)}\alpha_y \sin(\{^{(w)}\alpha_z) - \{^{(w)}\alpha_x \cos(\{^{(w)}\alpha_z)) \quad (8)$$

$$M^{(w)}\ddot{r}_z = \mathbf{p}_z^T \mathbf{F}_T - Mg \quad (9)$$

$$\begin{aligned} {}^{(\text{CoG})}I^{(w)}\ddot{\boldsymbol{\alpha}} &= [\mathbf{p}_y \quad \mathbf{p}_x \quad \mathbf{p}_c]^T \mathbf{F}_T - {}^{(\text{CoG})}\mathbf{w} \times {}^{(\text{CoG})}I^{(\text{CoG})}\mathbf{w} \\ \mathbf{p}_z &= [1 \quad \cdots \quad 1]^T; \quad \mathbf{p}_x = [-{}^{(\text{CoG})}r_{x_1} \quad \cdots \quad -{}^{(\text{CoG})}r_{x_N}]^T \\ \mathbf{p}_y &= [{}^{(\text{CoG})}r_{y_1} \quad \cdots \quad {}^{(\text{CoG})}r_{y_N}]^T; \quad \mathbf{p}_c = [c_1 \quad \cdots \quad c_N]^T \end{aligned} \quad (10)$$

Note that the translational accelerations  $\{^{(w)}\ddot{r}_x$  and  $\{^{(w)}\ddot{r}_y$  are the consequence of a roll  $\{^{(w)}\alpha_x$  and pitch  $\{^{(w)}\alpha_y$  tilt, which are the typical characteristics of an under-actuated system. Matrix  $P = [\mathbf{p}_z \quad \mathbf{p}_y \quad \mathbf{p}_x \quad \mathbf{p}_c]^T$  is used to represent the entire configuration of the multilinks

### 3.2. Attitude and altitude control based on linear-quadratic-integral control

**3.2.1. State equation for attitude and altitude.** In the case of the under-actuated system as described in Equations (7)–(10), the majority of existing works have focused on the linear map from the thrust force to the three-dimensional moment and collective force:  $P\mathbf{F}_T = [F \quad M] \in R^4$  (see Kumar and Michael, 2012) based on the first principal, and applied the dynamics inversion. In the inversion process, the desired moment  $M_{des}$  and the collective thrust  $F_{des}$  are first calculated based on the general feedback before the inverse mapping (e.g., Moore–Penrose pseudoinverse matrix) converts them into the target thrust forces  $F_{T_{des}}$ . Oung and D’Andrea (2014) extended such framework to an assemblable  $N$ -rotor system

using a scaling factor to circularly approximate the rotor configuration. The configuration in these related works is static, indicating the feedback gains are always constant. However, if the rotor configuration is variant, the same values of desired moment  $M_{des}$  and collective thrust  $F_{des}$  may result in unexpected desired thrust forces  $F_{T_{des}}$  (e.g., saturation of the thrust forces), because the inverse mapping changes as the configuration varies. Therefore, it is necessary to adjust feedback gains according to the varying forms.

Thus, a cost function is applied to the control framework with following motivations: (1) to obtain the optimized state feedback gains to ensure the asymptotic stability for dynamic configuration; (2) to guarantee the minimum control input effort (i.e., thrust force). The linear–quadratic–integral (LQI) control method as proposed by Young and Willems (1972) can then be introduced for attitude and altitude control.

The equations for the altitude and attitude (Equations (9) and (10), respectively) are first integrated to derive the transfer function from thrust forces  $\mathbf{F}_T$  to altitude and attitude:

$$\begin{aligned} \ddot{\mathbf{y}} &= P'\mathbf{F}_T - \mathbf{d} = \left[ \frac{1}{M}\mathbf{p}_z^T \quad {}^{(\text{CoG})}I^{-1}[\mathbf{p}_y \quad \mathbf{p}_x \quad \mathbf{p}_c]^T \right]^T \mathbf{F}_T - \mathbf{d} \\ \mathbf{y} &= [{}^{(w)}r_z \quad {}^{(w)}\alpha_x \quad {}^{(w)}\alpha_y \quad {}^{(w)}\alpha_z]^T; \\ \mathbf{d} &= [g \quad {}^{(\text{CoG})}I^{-1}({}^{(\text{CoG})}\mathbf{w} \times {}^{(\text{CoG})}I^{(\text{CoG})}\mathbf{w})]^T \end{aligned} \quad (11)$$

The offset term  $\mathbf{d}$  contains the static gravity force and the cross-product from the rotational dynamics. The static gravity force one can be regarded as the steady-state error and compensated by the LQI integral function, and thus has no influence on the later state equation. A feedforward

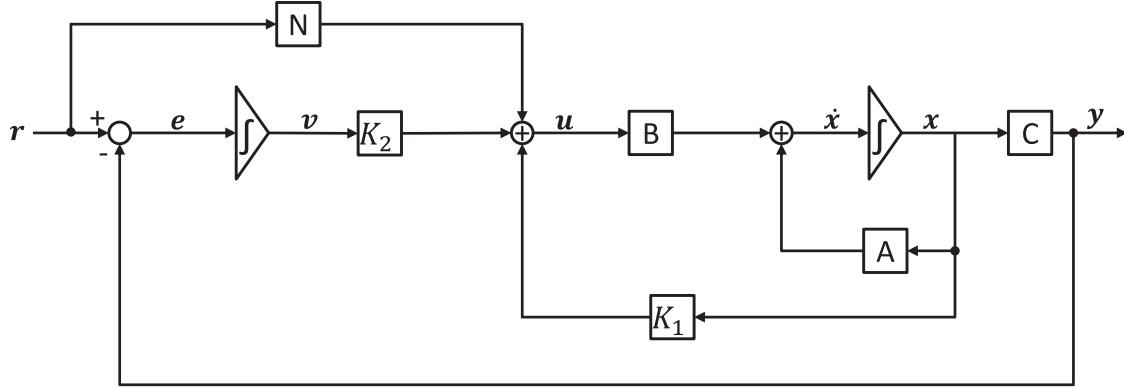


**Fig. 7.** The attitude and altitude control system based on the LQI control theory, which contains the output feedback, the reference feedforward, and state feedback controls.

compensation is then applied to the cross-product from rotational dynamics using the estimated angular velocity and inertia tensor:

$$\mathbf{F}_{comp} = P^\# [0 \quad {}^{CoG} \mathbf{w} \times {}^{CoG} I {}^{CoG} \mathbf{w}]^T \quad (12)$$

Here,  $\#$  denotes the pseudoinverse of the matrix. The cross-product can be confirmed to be compensated by substituting  $\mathbf{F}_{comp}$  into  $\mathbf{F}_T$  in Equations (9) and (10).

After defining a new control input  $\mathbf{u} = \mathbf{F}_T - \mathbf{F}_{comp}$ , the state equation for attitude and altitude in the LQI system with a new state

$$\mathbf{x} = [{}^W r_z \quad {}^W \dot{r}_z \quad {}^W \alpha_x \quad {}^W \dot{\alpha}_x \quad {}^W \alpha_y \quad {}^W \dot{\alpha}_y \quad {}^W \alpha_z \quad {}^W \dot{\alpha}_z]^T$$

can be written as

$$\dot{\mathbf{x}} = \mathbf{A} \mathbf{x} + \mathbf{B} \mathbf{u} \quad (13)$$

$$\mathbf{y} = \mathbf{C} \mathbf{x} \quad (14)$$

$$\mathbf{x} \in R^8, \quad \mathbf{u} \in R^N, \quad \mathbf{y} \in R^4$$

where

$$A = \begin{bmatrix} 0 & 1 & 0 & 0 & 0 & 0 & 0 & 0 \\ 0 & 0 & 0 & 0 & 0 & 0 & 0 & 0 \\ 0 & 0 & 0 & 1 & 0 & 0 & 0 & 0 \\ 0 & 0 & 0 & 0 & 0 & 0 & 0 & 0 \\ 0 & 0 & 0 & 0 & 0 & 1 & 0 & 0 \\ 0 & 0 & 0 & 0 & 0 & 0 & 0 & 0 \\ 0 & 0 & 0 & 0 & 0 & 0 & 0 & 1 \\ 0 & 0 & 0 & 0 & 0 & 0 & 0 & 0 \end{bmatrix};$$

$$B = [\mathbf{0} \quad \mathbf{p}'_z \quad \mathbf{0} \quad \mathbf{p}'_y \quad \mathbf{0} \quad \mathbf{p}'_x \quad \mathbf{0} \quad \mathbf{p}'_c]^T;$$

$$C = \begin{bmatrix} 1 & 0 & 0 & 0 & 0 & 0 & 0 & 0 \\ 0 & 0 & 1 & 0 & 0 & 0 & 0 & 0 \\ 0 & 0 & 0 & 0 & 1 & 0 & 0 & 0 \\ 0 & 0 & 0 & 0 & 0 & 0 & 1 & 0 \end{bmatrix}$$

Here,  $P' = [\mathbf{p}'_z \quad \mathbf{p}'_y \quad \mathbf{p}'_x \quad \mathbf{p}'_c]^T$ . Although the elements in  $B$  change with the transformation, the state equation models the system as a linear time-invariant system at each time point. In Equations (13) and (14),  $\mathbf{u}$  and  $\mathbf{y}$  are the input and output of the control system, respectively.

**3.2.2. Design of the LQI control framework.** As shown in Figure 7, the attitude and altitude control system comprises the output feedback, reference feedforward control, and state feedback control. As in previous work, the goal is to obtain the optimal gain matrix  $N, K_1, K_2$  on the basis of the LQI multivariable servo systems (Pak et al., 1974).

The state equation can then be extended by modifying the state and input, given by

$$\tilde{\mathbf{x}} \equiv \mathbf{x} - \mathbf{x}_s; \quad \tilde{\mathbf{u}} \equiv \mathbf{u} - \mathbf{u}_s \quad (15)$$

where  $\mathbf{x}_s$  and  $\mathbf{u}_s$  are the final values at the steady state.

As shown in

$$\dot{\tilde{\mathbf{v}}} = \mathbf{e} = \mathbf{r} - \mathbf{y} = \mathbf{C} \mathbf{x}_s - \mathbf{C} \mathbf{x} = -\mathbf{C} \tilde{\mathbf{x}} \quad (16)$$

we also introduce a tracking error  $\mathbf{e}$  between the reference input and the system output, along with its integral value  $\mathbf{v}$

Based on the extended state equation given by

$$\dot{\tilde{\mathbf{x}}} = \bar{A} \tilde{\mathbf{x}} + \bar{B} \tilde{\mathbf{u}} \quad (17)$$

$$\tilde{\mathbf{x}} = [\tilde{\mathbf{x}} \quad \mathbf{v}]; \quad \bar{A} = \begin{bmatrix} \mathbf{A} & \mathbf{O}_{8,4} \\ -\mathbf{C} & \mathbf{O}_{4,4} \end{bmatrix}; \quad \bar{B} = \begin{bmatrix} \mathbf{B} \\ \mathbf{O}_{4,N} \end{bmatrix}$$

the cost function can then be given by

$$J = \int_0^\infty (\tilde{\mathbf{x}}^T Q \tilde{\mathbf{x}} + \tilde{\mathbf{u}}^T R \tilde{\mathbf{u}}) dt \quad (18)$$

where  $Q$  and  $R$  are the positive semi-definite and positive-definite matrices, respectively, which affect the convergence characteristics of the control system.

The optimal input  $\mathbf{u}_0$  that provides the minimum cost can be obtained by solving the algebraic Riccati equation (ARE) given in

$$\bar{A}^T \Pi + \Pi \bar{A} + Q - \Pi \bar{B} R^{-1} \bar{B}^T \Pi = 0 \quad (19)$$

$$K \equiv [K_1 \ K_2] = -R^{-1} \bar{B}^T \Pi \quad (20)$$

$$\tilde{\mathbf{u}}_0 = K \bar{x} \quad (21)$$

Substituting  $\bar{x}$  into Equation (21) yields

$$\mathbf{u}_0 = K_1 \mathbf{x} + K_2 \mathbf{v} - K_1 \mathbf{x}_s + \mathbf{u}_s \quad (22)$$

Here, the last two terms are the feedforward part, the first of which improves the trackability to the reference input, and the second of which improves the convergence rate to the steady state. The term  $\mathbf{u}_s$  is neglected, as the two feedback terms already guarantee the asymptotic stability. Hence, the final input strategy for the attitude and altitude control system (Figure 7) can be derived as follows:

$$\mathbf{u}_0 = K_1 \mathbf{x} + K_2 \mathbf{v} + N \mathbf{r} \quad (23)$$

$$N = -K_1 C^T \quad (24)$$

Considering the compensation term for the cross-product mentioned in Equation (12), the desired thrust forces  $\mathbf{F}_{T_{des}}$  can be summarized as

$$\mathbf{F}_{T_{des}} = \mathbf{u}_0 + \mathbf{F}_{comp} \quad (25)$$

Here, the nominal thrust forces at the hovering state  $\mathbf{F}_{T_s} = \mathbf{u}_s$ , because the angular velocity is zero (and, thus,  $\mathbf{F}_{comp}$  is zero).

$$S_1 = \left\{ (\theta_1, \theta_2, \dots, \theta_N) | \theta_m = -\theta_{m+1} = \theta_0; m = 1, 3, 5, \dots; -\frac{\pi}{2} \leq \theta_0 \leq \frac{\pi}{2} \right\} \quad (28)$$

### 3.3. Position control in the horizontal plane

Position control for the horizontal motion uses the roll and pitch angles as inputs in a method similar to a backstepping approach (Bouabdallah and Siegwart, 2007).

The translational accelerations  ${}^{(w)}\ddot{r}_x$  and  ${}^{(w)}\ddot{r}_y$  are a consequence of pitch (7) and roll tilt (8), thus the relationship between the desired acceleration and desired roll and pitch angles can be written as

$$\begin{aligned} {}^{(w)}\alpha_{y_{des}} &= \frac{1}{g} ({}^{(w)}\ddot{r}_{x_{des}} \cos({}^{(w)}\alpha_z) + {}^{(w)}\ddot{r}_{y_{des}} \sin({}^{(w)}\alpha_z)) \\ {}^{(w)}\alpha_{x_{des}} &= \frac{1}{g} ({}^{(w)}\ddot{r}_{x_{des}} \sin({}^{(w)}\alpha_z) - {}^{(w)}\ddot{r}_{y_{des}} \cos({}^{(w)}\alpha_z)) \end{aligned} \quad (26)$$

where  $g$  is the acceleration constant due to gravity.

The desired accelerations  ${}^{(w)}\ddot{r}_{x_{des}}$  and  ${}^{(w)}\ddot{r}_{y_{des}}$  are calculated from a general proportional–integral–derivative (PID) controller:

$$\begin{aligned} {}^{(w)}\ddot{r}_{i_{des}} &= k_P ({}^{(w)}r_{i_{des}} - {}^{(w)}r_i) + k_I \\ &\int ({}^{(w)}r_{i_{des}} - {}^{(w)}r_i) d\tau + k_D ({}^{(w)}\dot{r}_{i_{des}} - {}^{(w)}\dot{r}_i) \end{aligned} \quad (27)$$

where the PID gains ( $k_P, k_I, k_D$ ) are adjusted to achieve the stable hovering position control.

### 3.4. Semi-stabilizable form and relaxed hover solution

**3.4.1. Singular and semi-stabilizable forms.** Let  $Y$  and  $F$  be defined as the sets of  $\mathbf{y}$  and  $\mathbf{F}_T$  ( $y \in Y, \mathbf{F}_T \in F$ ), respectively, and  $f$  as the mapping from  $F$  to  $Y$  ( $f : F \rightarrow Y$ ). According to Equations (9) and (10), if  $P$  has full rank, the mapping is surjective, indicating that the four elements in  $Y ({}^{(w)}r_z, {}^{(w)}\alpha_x, {}^{(w)}\alpha_y, {}^{(w)}\alpha_z)$  are independent of each other. If the Euler angles  ${}^{(w)}\alpha$  are multiplied by the inertia tensor on the left-hand side of Equation (10), the mathematical attribute of the mapping would not change, as the inertia tensor is a regular matrix. In contrast, the four elements cannot act independently, if  $P$  is not of full rank, leading to an uncontrollable result that is discussed later in this section.

We call the resulting special form the singular form. The rank of  $P$  can be calculated by checking the linear combination of row vectors ( $\mathbf{p}_z, \mathbf{p}_x, \mathbf{p}_y, \mathbf{p}_c$ ). It is evident that  $\mathbf{p}_z$  and  $\mathbf{p}_c$  are linearly independent because propellers are designed to spin in different directions in this work. Consequently, the linear independence of the two groups ( $\{\mathbf{p}_z, \mathbf{p}_x, \mathbf{p}_y\}$  and  $\{\mathbf{p}_c, \mathbf{p}_x, \mathbf{p}_y\}$ ) must be checked.

The vectors in the first group,  $\{\mathbf{p}_z, \mathbf{p}_x, \mathbf{p}_y\}$ , would be linearly dependent if and only if the lifting points act on a line, i.e., if there is a straight line across all propellers, as shown in Figure 8(a). This type of singular form can be summarized as a set described as

$$S_1 = \left\{ (\theta_1, \theta_2, \dots, \theta_N) | \theta_m = -\theta_{m+1} = \theta_0; m = 1, 3, 5, \dots; -\frac{\pi}{2} \leq \theta_0 \leq \frac{\pi}{2} \right\} \quad (28)$$

It is obvious that either the roll or pitch axis is not controllable in this case, indicating position control is difficult unless the relaxed definition of hovering proposed by Mueller and D’Andrea (2016) is employed. The relaxed hover solution involves the periodic angular velocity and acceleration. One matter of concern to apply this solution is the rigidity of a multilinked structure. The multilinked form may change owing to the centrifugal force under the fast rotating situation and cannot satisfy the periodic motion. Consequently, the aerial robot is not allowed to perform the form belonging to  $S_1$  in this work.

The vectors in the second group,  $\{\mathbf{p}_c, \mathbf{p}_x, \mathbf{p}_y\}$ , are linearly independent, except when  $N < 6$ , as the signs of the elements for the even and odd numbers of  $\mathbf{p}_c$  are opposite. Thus, two parallel straight lines must exist, one across all odd-numbered propellers and one across all even-numbered propellers, for linear dependence in this group. This is impossible when six links or more are used, unless all of the propellers are arranged in a line. However, when  $N = 4$ , the form shown in Figure 8(b) satisfies this precondition. In this case, the angles of all joints can be represented as

$$S_2 \supset \left\{ (\theta_1, \theta_2, \theta_3) | \theta_1 = -\theta_3 = \theta_0, \theta_2 = 0; -\frac{\pi}{2} \leq \theta_0 \leq \frac{\pi}{2} \right\} \quad (29)$$

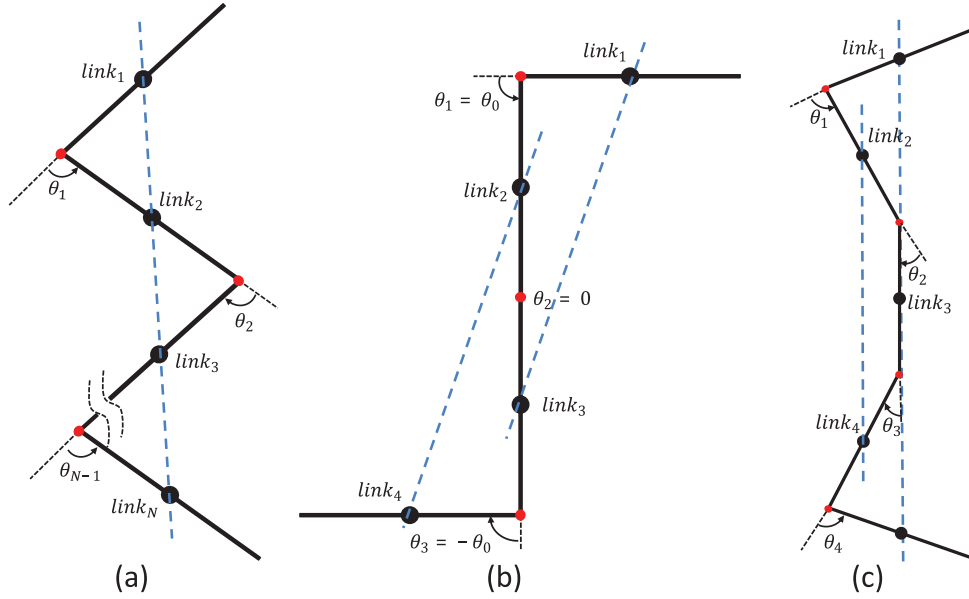


**Fig. 8.** Different singular forms: (a) a general singular form for any number of links, wherein the joint angles satisfy Equation (28); (b) a special singular form when  $N=4$ , wherein the joint angles satisfy Equation (29); and (c) a special singular form when  $N=5$ , wherein the joint angles satisfy Equation (30)

When  $N=5$ , the precondition is also satisfied by the formation shown in Figure 8(c). Applying the law of sines, the angles of all joints can then be represented as

$$\begin{aligned} S_2 \supset & \{(\theta_1, \theta_2, \theta_3, \theta_4) | 2 \sin(\theta_2) \\ & = \sin(\theta_1 - \theta_2), \theta_1 = \theta_3, \theta_2 = \theta_4\} \end{aligned} \quad (30)$$

This type of singular form can be described as the set  $S_2$ . Note that when the propellers are arranged in a line, the form belongs to both  $S_1$  and  $S_2$ . In the case of  $S_2$ , the vectors  $\{\mathbf{p}_z, \mathbf{p}_x, \mathbf{p}_y\}$  are independent, resulting in difficulties in yaw axis control. However, the position control can be still achieved, given that the pitch and roll axes are controllable. We define this form as semi-stabilizable and the corresponding relaxed hovering control method is presented later in this section. The free yaw motion may make the translational motion unstable, because of the centrifugal force mentioned previously. However, a short duration flight is still available. Therefore, it is allowed to pass this semi-stabilizable form while performing the aerial transformation.

**3.4.2. State in which the thrust force falls outside the valid range.** The thrust forces at the hovering state  $\mathbf{F}_{T_s}$  can be obtained by solving the statics problem:

$$\mathbf{g} = P(\boldsymbol{\theta})\mathbf{F}_{T_s} \quad (31)$$

where  $\mathbf{g} = [Mg, 0, 0, 0]^T$ . The argument  $\boldsymbol{\theta}$  is added for  $P$ , because this configuration is influenced by the joint angles( $\boldsymbol{\theta}$ ). When  $N=4$  and  $P$  is full rank, this simultaneous linear equation has a unique solution for  $\mathbf{F}_{T_s}$ :  $\mathbf{F}_{T_s} = P^{-1}\mathbf{g}$ . However, for a system with more than four

links, a null space occurs, resulting in infinite solutions for  $\mathbf{F}_{T_s}$ . Among the infinite solutions, the best option would have all hover thrust vector  $\mathbf{F}_{T_s}$  components furthest from the lower and upper force limit, i.e., where the components are closest to each other. In such a situation, the thrust force has the largest range against the disturbances. Otherwise, the thrust force may easily saturate while compensating for the external force. Thus, this situation can be considered to be the most robust and corresponds to a minimum variance in the hovering thrust force. The corresponding optimization problem can then be derived as follows:

$$\min_{\mathbf{F}_{T_s}} (w_1 \mathbf{F}_{T_s}^T \mathbf{F}_{T_s} + w_2 \text{var}(\mathbf{F}_{T_s})) \quad \text{subject to } \mathbf{g} = P(\boldsymbol{\theta})\mathbf{F}_{T_s} \quad (32)$$

Here, the first term of the cost function is added to minimize the total size of the thrust force, because only the second variance term can lead to a significantly large value of the thrust force. The weight coefficients  $w_1$  and  $w_2$  used to balance the two terms are not important, as explained later in this section.

This variance can be written as

$$\text{var}(\mathbf{x}) = E(\mathbf{x}^2) - E(\mathbf{x})^2 \quad (33)$$

where the function  $E(x)$  is used to calculate the mean of the elements of  $x$  and the first term is equal to  $\frac{\mathbf{F}_{T_s}^T \mathbf{F}_{T_s}}{N}$ . The second term  $E(\mathbf{F}_{T_s})^2$  remains constant, as the sum of thrust force  $\mathbf{F}_{T_s}$  is equal to  $Mg$  at the hovering state.

Hence, the problem in Equation (32) can be redefined as

$$\min \mathbf{F}_{T_s}^T \mathbf{F}_{T_s} \quad \text{subject to } \mathbf{g} = P(\boldsymbol{\theta}) \mathbf{F}_{T_s} \quad (34)$$

The Lagrange multiplier can be written as

$$\mathbf{F}_{T_s} = P^T (PP^T)^{-1} \mathbf{g} \quad (35)$$

This derivation from the physical aspects coincides with the minimum-norm solution of the least-squares problem.

The term regarding the control input  $\mathbf{u}$  in the cost function (18) is presented in a quadratic form associated with  $R$ . However, in this work,  $R$  is designed as an identity matrix, such that this term can also be written as  $\tilde{\mathbf{u}}^T \tilde{\mathbf{u}}$ . As the linear quadratic method is used to minimize the cost function which includes the input, the input at the steady state ( $\mathbf{u}_s$ ) achieved by the LQI control system should be same as the solution calculated using the Lagrange multiplier  $\mathbf{F}_{T_s}$  (Equation (35)).

Given that the direction of force generated by a propeller is always the same, the thrust force cannot be negative. However, the optimized result from the LQI control method

$$A' = \begin{bmatrix} 0 & 1 & 0 & 0 & 0 & 0 \\ 0 & 0 & 0 & 0 & 0 & 0 \\ 0 & 0 & 0 & 1 & 0 & 0 \\ 0 & 0 & 0 & 0 & 0 & 0 \\ 0 & 0 & 0 & 0 & 0 & 1 \\ 0 & 0 & 0 & 0 & 0 & 0 \end{bmatrix}, \quad B' = \begin{bmatrix} \mathbf{0} \\ \mathbf{p}_z'^T \\ \mathbf{0} \\ \mathbf{p}_y'^T \\ \mathbf{0} \\ \mathbf{p}_x'^T \end{bmatrix},$$

$$C' = \begin{bmatrix} 1 & 0 & 0 \\ 0 & 0 & 0 \\ 0 & 1 & 0 \\ 0 & 0 & 0 \\ 0 & 0 & 1 \\ 0 & 0 & 0 \end{bmatrix}^T$$

Accordingly, the LQI control method can then be followed to obtain the optimal gain matrix as shown in Figure 7. As the yaw stability is neglected, the compensation term for the cross-product in the rotational dynamics is also modified as follows:

$$\mathbf{F}_{comp} = \tilde{P}^\# [0 \ (\{CoG\} \mathbf{w} \times \{CoG\} I^{CoG} \mathbf{w})(0) \ (\{CoG\} \mathbf{w} \times \{CoG\} I^{CoG} \mathbf{w})(1)]^T \quad (39)$$

cannot guarantee non-negativity. Theoretically, the elements of  $\mathbf{u}_s (= \mathbf{F}_{T_s})$  will diverge to infinity whereas the multilinks transform towards a singular form belonging to either set  $S_1$  or set  $S_2$ , indicating that some of the elements of  $\mathbf{u}_s (= \mathbf{F}_{T_s})$  would become negative during this transformation. Under such forms, the flight control for full-stability is impossible. However, omitting the yaw control allows the thrust force at the relaxed hovering state to be rewritten as

$$\mathbf{F}_{T_s} = \tilde{P}^T (\tilde{P} \tilde{P}^T)^{-1} \mathbf{g}'$$

$$\tilde{P} = [\mathbf{p}_z \ \mathbf{p}_x \ \mathbf{p}_y]^T; \quad \mathbf{g}' = [Mg \ 0 \ 0]^T \quad (36)$$

Thus, Equation (36) is the relaxed hovering thrust for the semi-stabilizable forms. In most cases, the relaxed  $\mathbf{F}_{T_s}$  is within the valid range of thrust force. However, if the form is closed to the first singular form  $S_1$ , the rank of  $\tilde{P}$  would decrease again, leading to the divergence of  $(\tilde{P} \tilde{P}^T)^{-1}$  (and, thus,  $\mathbf{F}_{T_s}$ ).

### 3.5. Relaxed hover solution without yaw control

The state equation with reduced state ( $\mathbf{x}' = [\{^W\} r_z \ \{^W\} \dot{r}_z \ \{^W\} \alpha_x \ \{^W\} \dot{\alpha}_x \ \{^W\} \alpha_y \ \{^W\} \dot{\alpha}_y]^T$ ) can be rewritten to control semi-stabilizable forms as follows:

$$\dot{\mathbf{x}}' = A' \mathbf{x}' + B' \mathbf{u} \quad (37)$$

$$\mathbf{y}' = C' \mathbf{x}' \quad (38)$$

$$\mathbf{x}' \in R^6, \quad \mathbf{u} \in R^N, \quad \mathbf{y}' \in R^3$$

where

## 4. Grasp-form searching method for two-dimensional multilinks

Regarding the grasping task, the entire multilinked structure can be regarded as a planar gripper, of which the propeller duct serves as the gripper surface. Planar grasping requires the force-closure (Watanabe et al., 2006) to generate enough vertical friction to lift against gravity. In our work, the target object is limited to regular objects (a cylinder or a convex polygonal column) and should be smaller than the robot so that an enveloping grasp (and, thus, the force-closure) can be achieved. This section involves three parts: a recursive calculation method to retrieve the candidates of the grasp form with respect to the geometry of object and the kinematics of the multilinks; an analysis of the force-closure and hovering state conditions for the candidate form obtained from the candidates; and a full search method to find the best range of grasping form that takes the joint torque and the hovering thrust forces into consideration.

### 4.1. Recursive calculation method to retrieve enveloping grasp form

We assume that all links are in contact with the object, and this provides a more stable closure for the target object. As mentioned, all objects are assumed to have a convex polygonal column or cylinder shape, which guarantees the same sign for all joint angles while they are enveloping the object. Recursive calculation aims to retrieve the joint

angles  $\theta$  constructing a valid enveloping form and the position of all contact points:  $[\mathbf{P}_{c_1}, \dots, \mathbf{P}_{c_N}]$ . Different algorithms are developed for convex polygonal columns and cylinders.

**4.1.1. Cylinder.** As shown in Figure 9(a), the cross-section of the object is a circle of radius  $R_{object}$ . It is obvious that  $\delta_{i+1} = -\delta_i$ , owing to the geometry of circle ( $\delta_i$  is the angle between the link and the tangential line cross the contact point  $\mathbf{P}_{c_i}$ ). Therefore, the joint angles and contact points are easily retrieved from planar geometry using the law of cosines and sines. The valid joint angle  $\theta_i$  should not be smaller than zero. If  $\theta_1 = 0$ , an isosceles triangle consisting of  $\mathbf{P}_O$ ,  $\mathbf{P}_{L_1}$ , and  $\mathbf{P}_{L_2}$  is built. Then the angle between  $link_i$  and the tangent line passing through  $\mathbf{P}_{C_i}$  is equal to  $\angle \mathbf{P}_{L_1} \mathbf{P}_O \mathbf{P}_{J_1}$ , found by  $\sin^{-1}\left(\frac{l_L}{2(R_{object} + R_{duct})}\right)$ . This value forms the upper bound of the initial variable  $\delta_1$ , whereas the negative of the upper bound forms the lower bound. Thus, the fundamental range for the initial variable is  $\left[-\sin^{-1}\left(\frac{l_L}{2(R_{object} + R_{duct})}\right), \sin^{-1}\left(\frac{l_L}{2(R_{object} + R_{duct})}\right)\right]$ .

**4.1.2. Convex polygonal column.** This object's cross-section is a convex polygon described by  $[\psi_1, \dots, \psi_N]$  and  $[l_{S_1}, \dots, l_{S_N}]$ , where  $\psi_i$  and  $l_{S_i}$  are the vertex angle and side length, respectively, as shown in Figure 9(b). Different links are assumed to only contact with different sides, i.e.,

a side should only contain one contact point. In addition, the number of the sides is assumed equal to the number of links. The joint angle  $\theta_i$  can then be retrieved based on the geometry of the polygon and the kinematics of the multilinks, as shown in Figure 9(b). The previous contact point  $\mathbf{P}_{c_i}$  is set as the local origin to calculate  $\theta_i$ . The joint angle with the next contact point  $\mathbf{P}_{c_{i+1}} = [x_{c_{i+1}}, y_{c_{i+1}}]$  can then be expressed in the local frame as follows:

$$\begin{cases} x_{c_{i+1}} = R_{duct}(\cos \psi_i - 1) + \frac{l_L}{2}(\sin \delta_i + \sin(\delta_i + \theta_i)) \\ y_{c_{i+1}} = R_{duct} \sin \psi_i - \frac{l_L}{2}(\cos \delta_i + \cos(\delta_i + \theta_i)) \end{cases} \quad (40)$$

where  $l_L$  and  $R_{duct}$  are the length of the link and the radius of the propeller duct, respectively, and  $\delta_i$  is the angle between the link and the corresponding polygon side.

In addition, point  $\mathbf{P}_{c_{i+1}}$  has the following feature:

$$x_{c_{i+1}} = \tan \psi_i(-y_{c_{i+1}} - d_i) \quad (41)$$

where  $d_i$  is the distance from the contact point  $\mathbf{P}_{c_i}$  to the vertex point  $\mathbf{P}_{v_i}$ .

The joint angle  $\theta_i$  can then be calculated by substituting Equation (41) into Equation (42). Subsequently,  $\delta_{i+1}$  and  $d_{i+1}$  can be retrieved for the next routine. Thus, the calculation process recursively conducts from  $i=1$  to  $i=N-1$  with the given initial variables  $\delta_1$  and  $d_1$ . Unexpected results generating invalid forms in the multilinked kinematics, such as  $d_i \leq 0$  or  $d_i \geq l_{S_i}$ , are also accounted for. For these situations, the recursive processes stop.

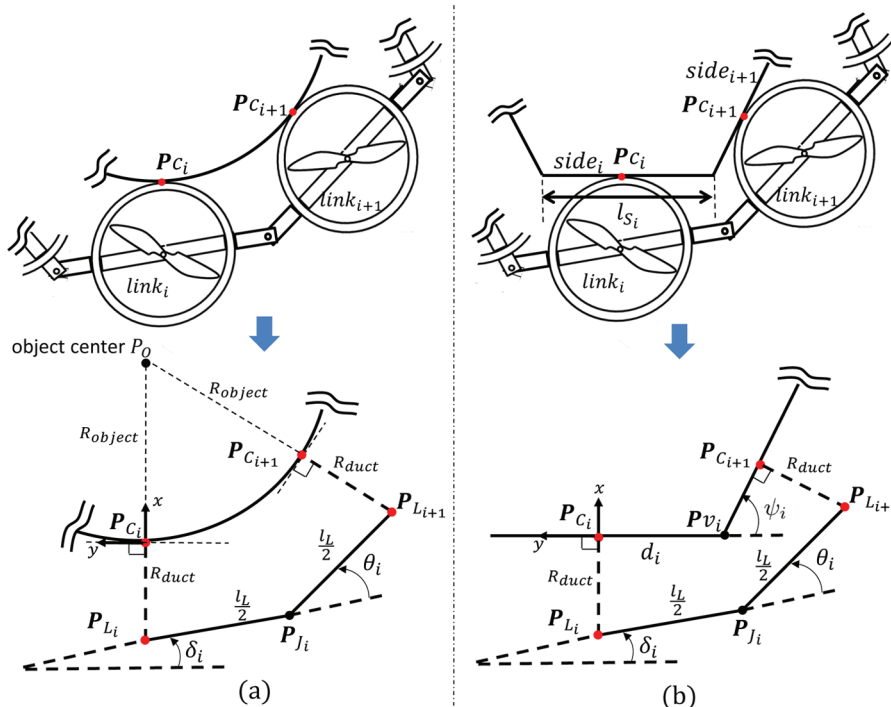


**Fig. 9.** The whole-body enveloping rule according to multilinks kinematics and the geometry of the target object: (a) enveloping a cylindrical object and (b) enveloping a convex polygonal column. The joint angle  $\theta_i$  can be retrieved recursively.

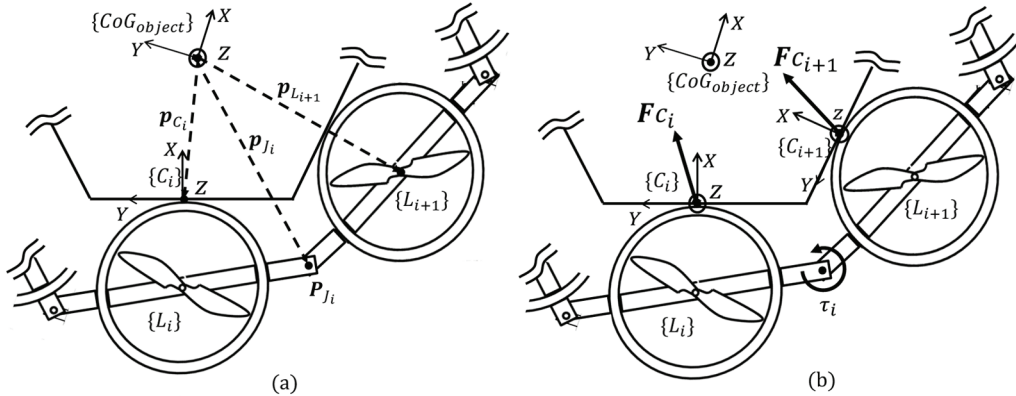


**Fig. 10.** (a) Kinematics of the target object and multilinks based on force-closure, where  $\mathbf{p}_{c_i}$ ,  $\mathbf{p}_{L_i}$ , and  $\mathbf{p}_{J_i}$  are the position of the contact point, the link, and joint expressed in the object frame  $\{\text{CoG}\}$ , respectively. (b) Statics of target object and multilinks, where  $\mathbf{F}_i$  and  $\tau_i$  are the contact force and joint torque, respectively.

#### 4.2. Statics of object and two-dimensional multilinks based on force-closure

**4.2.1. Contact forces based on force-closure.** The statics model of the object associated with the contact forces can be considered as a force-closure problem (Watanabe et al., 2006). As shown in Figure 10(b), the contact force can be written as  $\mathbf{F}_{c_i} = [F_{c_{ix}}, F_{c_{iy}}, F_{c_{iz}}]^T$  expressed in the contact point frame  $\{c_i\}$ , with a range of  $F_{c_{ix}} \geq 0$ ;  $(F_{c_{iy}}^2 + F_{c_{iz}}^2) \leq \mu^2 F_{c_{ix}}^2$ , where  $\mu$  is the coefficient of friction. The force of gravity must be considered on the grasped object being held in the air. The aerial robot (and, thus, the object) are assumed to not accelerate, and thus the z-axis points upwards. Thus, the statics of the object with respect to the  $\{\text{CoG}\}$  frame can be described as follows:

$$G_c \mathbf{F}_{FC} + \mathbf{F}_e = 0 \quad (42)$$

$$\begin{aligned} G_c &= [G_{c_1} \dots G_{c_N}] \in R^{6 \times 3N} \\ G_{c_i} &= [\mathbf{R}_{c_i}, [\mathbf{p}_{c_i} \times] \mathbf{R}_{c_i}]^T \in R^{6 \times 3} \\ \mathbf{F}_{FC} &= [\mathbf{F}_{c_1}^T, \dots, \mathbf{F}_{c_N}^T]^T \in R^{3N} \\ \mathbf{F}_e &= [0, 0, -mg, 0, 0, 0]^T \end{aligned}$$

where  $\mathbf{R}_{c_i}$  and  $\mathbf{p}_{c_i}$  are the orientation of the contact point frame  $\{c_i\}$  and the position of contact point expressed in the  $\{\text{CoG}\}$  frame, respectively, as shown in Figure 10(a). In addition, note that  $m$  is the mass of the target object and  $N$  is the number of contact points, which is equal to the number of links.

Minimizing the norm of the vector integrated from the  $F_{c_{ix}}$  and  $F_{c_{iy}}$  elements in  $\mathbf{F}_{FC}$  provides the minimum load of joint torque under the given enveloping form. To linearize the minimization problem, the friction cone model is approximated to a four-sided pyramid, where  $F_{c_{ix}} \geq 0$ ,  $|F_{c_{iy}}| < \mu F_{c_{ix}}$ ,  $|F_{c_{iz}}| < \mu F_{c_{ix}}$ . Therefore, the problem to find the minimum norm of contact force can be described as in the following equation and the optimization problem can be solved by applying the general QP algorithm (Ferreau et al., 2014):

$$\begin{aligned} \min_{\mathbf{F}_{FC}} \quad & \mathbf{F}_{FC}^T H \mathbf{F}_{FC} \\ \text{s.t.} \quad & G_c \mathbf{F}_{FC} + \mathbf{F}_e = 0 \\ & G_{fric} \mathbf{F}_{FC} \geq 0 \end{aligned} \quad (43)$$

where

$$\begin{aligned} H &= \text{diag}[h_i]; \quad G_{fric} = \text{diag}[g_{fric_i}] \in R^{5N \times 3N} \\ h_i &= \begin{bmatrix} 1 & 0 & 0 \\ 0 & 1 & 0 \\ 0 & 0 & 0 \end{bmatrix}; \quad g_{fric_i} = \begin{bmatrix} 1 & 0 & 0 \\ \mu_1 & -1 & 0 \\ \mu_1 & 1 & 0 \\ 0 & 0 & 1 \\ \mu_2 & 0 & -1 \end{bmatrix} \end{aligned}$$

**4.2.2. Joint torque based on statics.** Although the aerial robot moves in the air, the multilinks are relatively static with respect to the object  $\{\text{CoG}\}$  frame, as all the contact points should not move with respect to the object surface. Hence, the joint torque  $\tau$  can be retrieved with the principle of virtual work (Tsai, 1999) as described in

$$\begin{aligned} \tau &= - \sum_{i=1}^N J_{B_i}^T(\boldsymbol{\theta}) G_{c_i} \mathbf{F}_{c_i} \\ J_{B_i} &= [J_{B_{i1}}, \dots, J_{B_{ij}}, \dots, J_{B_{iN-1}}] \\ J_{B_{ij}} &= \begin{cases} \left[ [e_z \times] (\mathbf{p}_{c_j} - \mathbf{p}_{J_i}) \right] & (i > j) \\ e_z & (i = j) \\ 0 \in R^6 & (i \leq j) \end{cases} \end{aligned} \quad (44)$$

where  $e_z = [0, 0, 1]^T$  is the unit vector of the rotation direction, and  $j$  represents the index of the joint,  $1 < j < N - 1$ . According to Equation (43), it is thus possible to find minimum contact force exerted in object with force-closure. Then we can also retrieve the corresponding joint torque from Equation (44).

**4.2.3. Hovering thrust forces while grasping.** Analyzing the hovering state after grasping is also important. It can be assumed that object remains relatively static in the multi-linked aerial robot system (and, thus, the robot  $\{CoG\}$  frame). According to the transformation from the object and aerial robot, a regular forward kinematics adding the object as a static module to the multilinked structure can easily be performed. The addition of the object would influence the relative position of the robot  $\{CoG\}$  frame and, thus, the rotor configuration and the total mass. Updating the configuration matrix  $P$  and vector  $g$  in Equation (35) gives the modified hovering thrust forces  $\mathbf{F}_{T_s}$  during grasping.

### 4.3. Optimal grasping form based on the full search method

There are two important aspects regarding form searching: joint torque and hovering thrust force. Regarding the joint torque, the goal is to suppress the maximum component of the joint torque  $\boldsymbol{\tau}$  from Equation (44). The lower the maximum component is, the more extra torque can be yielded from the servo motor to generate more internal forces. Meanwhile, the cost function (34) can be applied to compare the stability or robustness of hovering thrust force among various candidate grasping forms.

Given that the relationship between the initial variables, such as  $d_1$  and  $\delta_1$ , and the joint torque is highly nonlinear, it is difficult to apply the general linear optimal planning method. Therefore, a full search method employing a certain resolution for each initial variable is developed. A weighted sum function is introduced into the cost function for each candidate:

$$cost(init\_vars) = w_1 \max(\boldsymbol{\tau}) + w_2 \|\mathbf{F}_{T_s}\| \quad (45)$$

where  $\max(\boldsymbol{\tau})$  denotes the maximum component of  $\boldsymbol{\tau}$ , and  $\max(\boldsymbol{\tau})$  and  $\mathbf{F}_{T_s}$  can be regarded as a function of the initial variables (*init\_vars*).

Sensor noise and model error must be taken into account in the real situation. As such, it is more practical to search for the best range of grasping forms, rather than a single optimal solution. All grasping forms within this range are considered valid.

Thus, the goal of the searching process is to find the area  $\bar{S}$  with the minimum summed cost, as described in Equation (45) defined as the best grasping form range:

$$\bar{S} = \arg \min_S \sum_{init\_vars \in S} cost(init\_vars) \quad (46)$$

where  $S$  denotes the area over which to calculate the sum of the cost. The form corresponding to the center of the best area is, thus, the best grasp form  $\boldsymbol{\theta}_{des}$ .

In summary, this procedure: (a) collects the valid enveloping form candidates with their corresponding joint angles  $\boldsymbol{\theta}$  from the given initial variables; (b) estimates the contact force  $\mathbf{F}_{FC}$  with minimum norm and their corresponding

joint torque  $\boldsymbol{\tau}$  as well as the hovering thrust force  $\mathbf{F}_{T_s}$  for each form candidate; (c) records the cost calculated by Equation (45) for each candidate; and (d) finds the area with the minimum summed cost as described in Equation (46) by a full searching method on all candidates. If a candidate is determined invalid in step (a) or (b), it is assigned an infinite cost, guaranteeing its removal from the global solution.

### 4.4. Searching result on cylindrical and box-type objects

We demonstrate the searching results to find the best grasp form on a cylindrical and box-type object, based on the quadrotor with four links that has the same specification as presented in Tables 1 and 2. Regarding the basic configuration of the multilinks,  $l_L$  and  $R_{duct}$  are 0.6 and 0.2 m, respectively. The weight of aerial robot and target object are 3.34 and 1.0 kg, respectively. The coefficient of friction is assumed to be 0.3, which is a general value in the real situation. The weights assigned to joint torque  $w_1$  and hovering thrust force  $w_2$  in Equation (45) are both set to 0.5.

**4.4.1. Cylindrical object.** In this case there is only one initial variable  $\delta_1$ . In this searching problem, the diameter of the cylinder is set to 0.25 m. The window size of the only initial variable  $\delta$  is set to 0.087 rad. The best grasping form found from the proposed searching method is shown in Figure 11(a); Figure 12 shows the changes of the maximum component of  $\boldsymbol{\tau}$ , the maximum component of  $\mathbf{F}_{T_s}$ , the minimum component of  $\mathbf{F}_{T_s}$ , and the cost value, as described by Equation (45). The red area indicates the best grasping form range ( $\delta_1 \in [-0.0730, 0.014]$ ), and the lower and upper bounds of the valid grasping forms are found to be  $\underline{\boldsymbol{\theta}} = [1.569, 1.412, 1.569]$  and  $\bar{\boldsymbol{\theta}} = [1.476, 1.506, 1.476]$ , respectively. The best grasp form found is  $\boldsymbol{\theta}_{des} = [1.523, 1.459, 1.523]$ . At the best form, the minimum torque required to hold the object in the air is  $\tau = [1.600, 3.186, 1.600]$ , and the hovering thrust force is  $\mathbf{F}_{T_s} = [9.685, 11.626, 11.587, 9.646]$ . Only slight changes are seen in  $\max(\boldsymbol{\tau})$ ,  $\max(\mathbf{F}_{T_s})$ , and  $\min(\mathbf{F}_{T_s})$ , possibly because the range of candidate forms is small and the relative position between the cylinder and the multilinks seldom changes.

**4.4.2. Box-type object.** When the object is irregular, searches must be performed on each side of the polygon. However, a box with a square base only requires a search to be performed on one side. The side length of the object is 0.3 m, and the initial variables are  $\delta$  and  $d$ . We change these variables with respect to the third link (same orientation with  $\{CoG\}$  frame) instead of the first link for convenience in the approaching and grasping motion strategy presented in Section 5. Therefore, the recursive calculation method involves two branches: from the third link to first

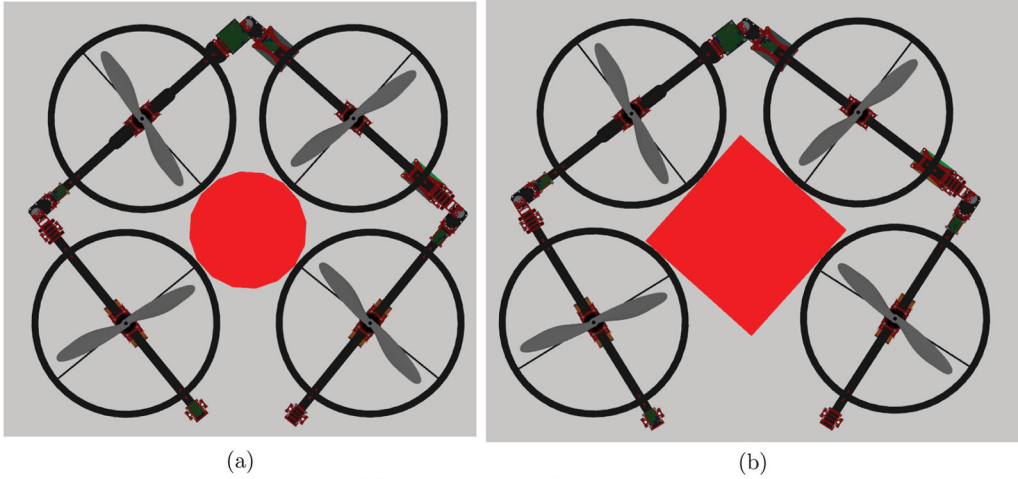


**Fig. 11.** The best forms to grasp (a) cylindrical and (b) box-type objects resulting from the proposed searching method.

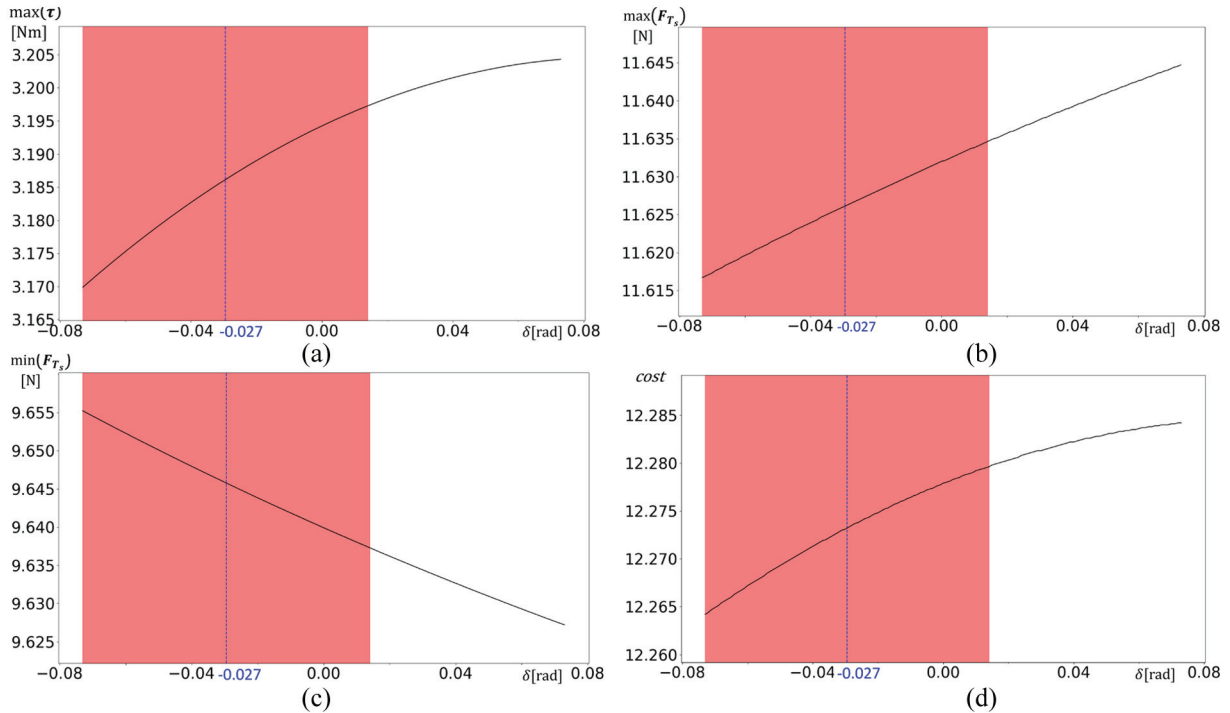


**Fig. 12.** Results of the proposed searching method to find the best form to grasp a cylindrical object using the quadrotor prototype: (a) the change of the maximum component in the vector of joint torque  $\tau$  while the angle  $\delta$  is changed, where  $\delta$  represents the angle between the link and the tangent link crossing the corresponding contact point, as shown in Figure 9(a); (b) the change of the maximum component in the vector of hovering thrust  $F_{T_s}$  while grasping the object and hovering; (c) the change of the minimum component in the vector  $F_{T_s}$ ; and (d) the change of the cost, as described by Equation (45). The red area and the blue dashed line correspond to the valid grasping form range and the best grasp form, respectively, as described by Equation (46)

link and fourth link ( $3 \rightarrow 1$ ,  $3 \rightarrow 4$ ), and the analysis on force-closure and hovering state follows the regular routine. The window size for searching is set to  $d = 0.03$  m and  $\delta = 0.087$  rad.

Figure 11(b) demonstrates the best grasping form resulting from the proposed searching method. Figure 13 shows the changes of the maximum component of  $\tau$ , the

maximum component of  $F_{T_s}$ , the minimum component of  $F_{T_s}$ , and the change of the cost value, as described by Equation (45). The red area indicates the best grasping form range ( $\delta_3 \in [\underline{\delta}_3, \bar{\delta}_3] = [-0.225, -0.138]$ ;  $d_3 \in [\underline{d}_3, \bar{d}_3] = [0.105, 0.135]$ ). The lower and upper bounds of the valid grasping forms are found to be  $\underline{\theta} = [1.500, 1.304, 1.447]$  and  $\bar{\theta} = [1.484, 1.307, 1.480]$ .

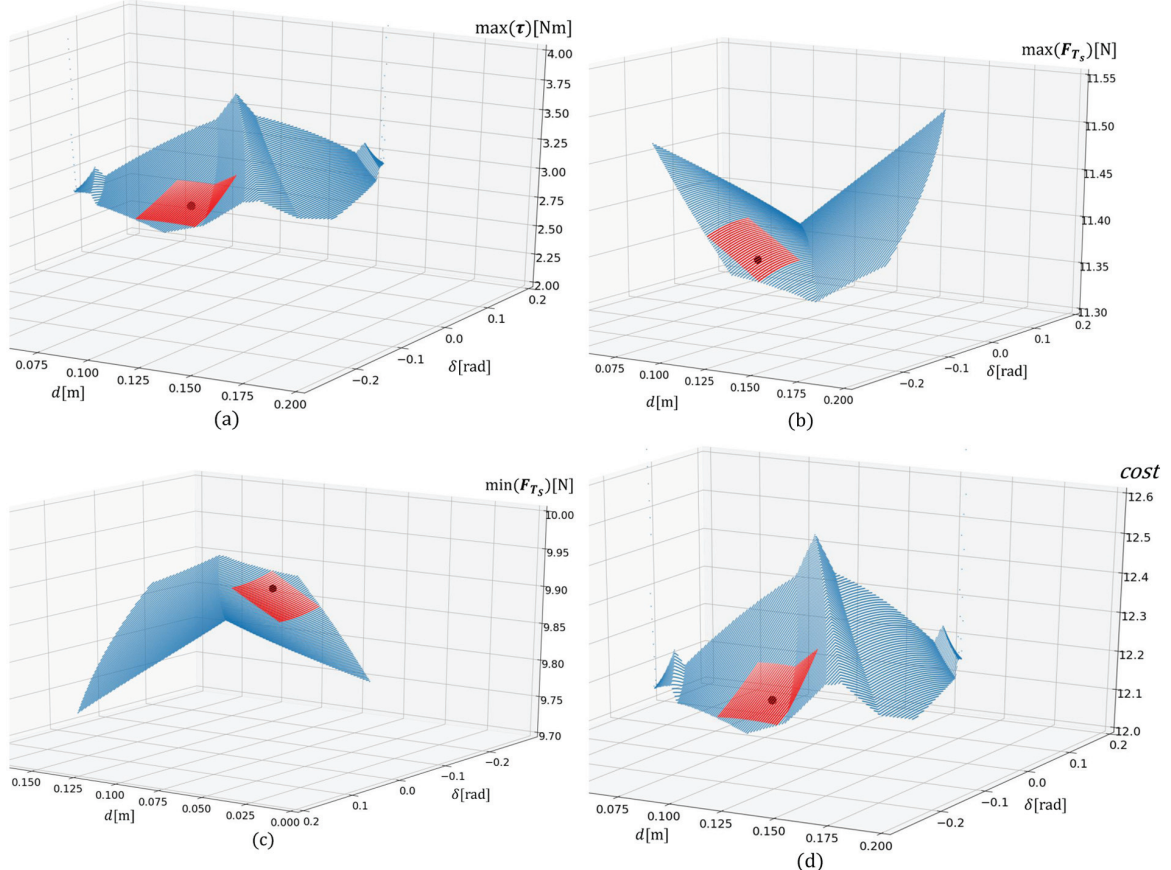


**Fig. 13.** Results of the proposed searching method to find best form to grasp a box-type object using the quadrotor prototype: (a) the change of the maximum component in the vector of joint torque  $\tau$  while the angle  $\delta$  is changed, where  $\delta$  represents the angle between the link and the tangent link crossing the corresponding contact point, as shown in Figure 9(a); (b) the change of the maximum component in the vector of hovering thrust  $F_{T_s}$  while grasping the object and hovering; (c) the change of the minimum component in the vector  $F_{T_s}$ ; and (d) the change of the cost, as described by Equation (45). The red area and the blue dashed line correspond to the valid grasping form range and the best grasp form, respectively, as described by Equation (46). The view angle of the plot (c) is different from other plots, resulting in the relative different position of the red area.

The best grasp form found is  $\theta_{des} = [1.493, 1.306, 1.465]$ . At the best form, the minimum torque required to hold the object in the air is  $\tau = [1.782, 3.094, 1.201]$  and the hovering thrust force is  $F_{T_s} = [9.883, 11.319, 11.389, 9.953]$ . The change tendency of  $\max(\tau)$  and  $F_{T_s}$  are different, and the tendency of cost (Figure 13(d)) is similar to that of  $\max(\tau)$ . This is likely because the change of  $\max(\tau)$  is larger than the change of  $\max(F_{T_s})$  and  $\min(F_{T_s})$ .

## 5. Aerial approach and grasp motion strategy

The appropriate procedure to approach and grasp an object is important for any object-picking task. We assume that the object shape and position are well-known. As such, the desired grasping form can be calculated in advance using the searching method described in Section 4. Hence, the goal of grasping is to reach the desired contact points with the desired grasp form, presenting a planar grasping control problem. One general solution involves minimizing the

distance between the desired contact points and the corresponding points on the ducts of the propeller. However, position control is difficult because the high turbulence generated by the floor and the object cannot be ignored. In the adaptive grasping motion proposed in our previous work (Zhao et al., 2017), the multilinked aerial robot first hovers and envelops the object in an extended form without contacting the object before slowly changing to the desired grasping form. Given that the aerial robot is floating, the robot can perform relative motions towards the target object and adapt to the object shape under the final desired form. Two types of relative motions between the propeller duct and the surface of the object exist: a rolling motion without kinetic friction and a slipping motion with kinetic friction. The previous adaptive grasping motion depends heavily on the slipping motion. If the coefficient of static friction is large and the normal force exists after contact, the corresponding duct remains entirely on the object at the contact point. If there are two such contact points, the multilinks remain against the object, and the grasping motion stops in

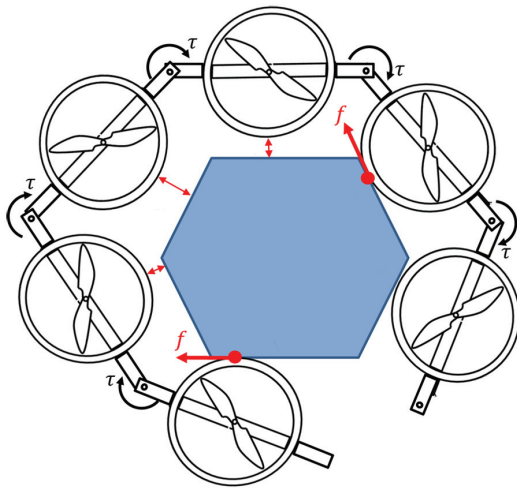


**Fig. 14.** Previous approach and grasp method that depends on the slipping motion between the duct and the object's surface and may become stuck if the joint torque  $\tau$  cannot exceed the value of the fiction  $f$  at the contact points.

the middle, as the joint torque cannot overcome the high static friction. In this case, as shown in Figure 14, some ducts cannot contact the object. Under this situation, the force-closure is not achieved, and the object cannot be picked up.

Therefore, an improved approach and grasp motion strategy to guarantee full contact under the desired grasping form is proposed in this paper. The key point is the first two contacts made by the two continuous links, as shown Figure 15. The joint connecting these links is defined as the center joint. For cylindrical objects, if the angle of the center joint is equal to the desired value for grasping and the links on both sides are in contact with the object, the contact points are also correct. On the other hand, convex polygonal columns require two variables ( $d$  and  $\delta$ ) to

determine contact points, as shown in Figure 9(b). However, if the joint angle is fixed, either of the two initial variables can be uniquely determined by adjusting the other. Taking the advantage of the rolling motion of the duct on the surface of the object, the angle  $\delta$  is much easier to adjust by the yaw control of the aerial robot than the other variable,  $d$ . Assuming the angle  $\delta$  coincides with the desired value, these two links satisfy the contact condition of the desired situation under the desired grasp form. Thus, the approach phase has ended, and the subsequent grasp motion begins from both sides of the center joint. The final grasp form is theoretically identical to the desired grasp form, which is the straightforward result of the recursive calculation method, as shown in Figure 9(b).

The overall motion sequence is summarized in Figure 16, which is separated into three phases: the approach, grasp, and closure phases. The approach phase is further divided into three sub-phases: approach above the object, transform and descend, and approach to contact. Two main areas of improvement from our previous work exist: the third sub-phase of the approach phase (approach to contact) and the grasp phase. The following sections describe each phase.

### 5.1. Approach phase

The motion of the proposed multilinked aerial robot can be described as  $R^3 \times SO(2)$  if the joint angles are relatively fixed. However, stable positioning, especially horizontally, cannot be achieved when the robot is close to the floor or object because of the turbulence. Therefore, the approach phase is divided into three sub-phases to minimize this influence. The first two sub-phases are designed to reach the goal position and yaw angle  $({}^W r_x, {}^W \alpha_{z_{des}})$  as closely as possible. The third sub-phase is proposed to contact the object with the correct two points based on the acceleration control.

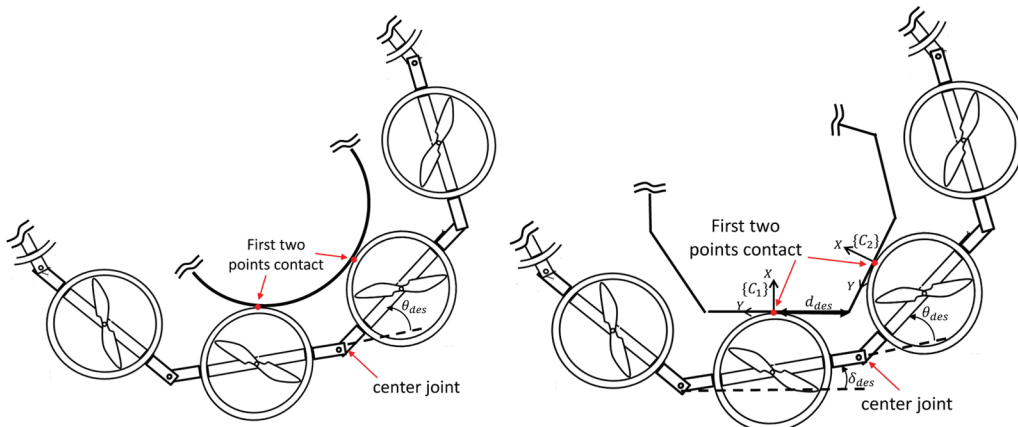


**Fig. 15.** Proposed approach motion. The key point is to achieve the first two points of contact by the two continuous links on both sides of the center joint. The desired angle of the center joint is set as  $\theta_{cj_{des}}$ , as is found in the proposed searching method described in Section 4.

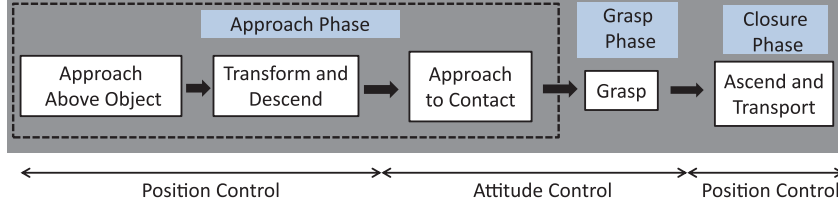


**Fig. 16.** A summary of the proposed motion sequence for the aerial approach and grasp motion.

**5.1.1. Approach above object.** Here, the robot moves closer to and hovers above the object. The height remains constant; therefore, the motion can be described as SE(2). This sub-phase provides convergence to the desired state in SE(2), because the turbulence from the floor and object can be ignored at this height. In addition, a downward-pointing camera can be used to recognize and to estimate the shape and position of the object. However, the position and shape of the object are assumed well-known for the purposes of this research and, thus, object recognition is not addressed.

**5.1.2. Transform and descend.** After the convergence of the position and yaw angle, the transformation begins. The goal form in this sub-phase is the relaxed form that envelops the object. However, only the center joint rotates to the desired grasp angle  $\theta_{cjdes}$ , which is important in the next sub-phase. A uniform additional angle  $\Delta\theta$  is introduced for the other joints and the approaching form can then be described as

$$\theta_{i_{approach}} = \begin{cases} \theta_{i_{des}} & (i = i_{cj}) \\ \theta_{i_{des}} - \Delta\theta & (\text{otherwise}) \end{cases} \quad (47)$$

where  $\theta_{i_{des}}$  is the optimized result obtained from the searching method described in Section 4. The desired horizontal position and yaw angle ( ${}^{(w)}r_{x_{des}}, {}^{(w)}r_{y_{des}}, {}^{(w)}\alpha_{z_{des}}$ ) in this sub-phase are identical to the first sub-phase and are already in place. Collision avoidance should be considered by projecting the aerial robot to the same height level as the object. The angle of the center joint during this sub-phase becomes already identical to the final closure phase. Thus, only a relative translational offset is necessary before the closure phase. Given the different geometric features between cylindrical and convex polygonal columns, different offset calculation methods are calculated as follows:

$$\text{Cylinder : } {}^{(w)}\mathbf{r}_{offset} = d_{offset} {}^{(w)}\hat{\mathbf{r}}_{P_o P_{cj}} \quad (48)$$

$$\text{Convex Polygonal Column : } {}^{(w)}\mathbf{r}_{offset} = -d_{offset}({}^{(w)}\mathbf{n}_{\{C_1\},y} + {}^{(w)}\mathbf{n}_{\{C_2\},y}) \quad (49)$$

where  $P_o$  and  $P_{cj}$  are the object center point and center joint point, respectively, as shown in Figure 17. For cylinders, the hat map  $\wedge$  for vector  $\mathbf{r}$  indicates a unit vector having the same direction as vector  $\mathbf{r}$ . For convex polygonal columns, the frame of the polygon cross-section side is defined as  $C_i$

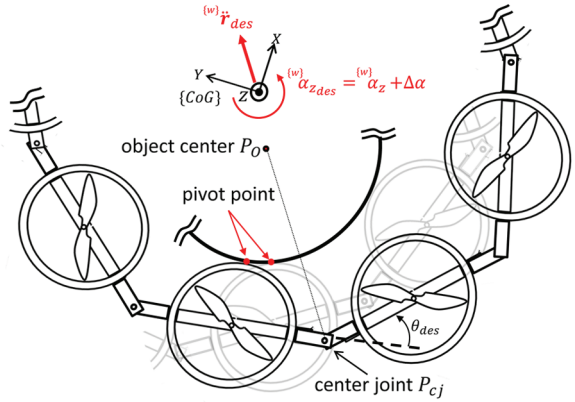


**Fig. 17.** The rolling motion on the surface of cylinder. The desired acceleration of the robot  ${}^{(w)}\ddot{\mathbf{r}}_{des}$  is parallel with the line segment from the center joint  $P_{cj}$  to the object center  $P_o$ , and the desired yaw angle  ${}^{(w)}\alpha_{z_{des}}$  contains the constant offset  $\Delta\alpha$ , resulting in contact at two points, as shown in the transparent form.

to be consistent with the definition given in Figures 9(b) and 10. The unit vector  ${}^{(w)}\mathbf{n}_{\{C_i\},y}$  represents the direction of the  $y$ -axis on the corresponding polygon side with reference to the world frame  $\{W\}$ , and  $d_{offset}$  is the scalar value of the offset distance. Defining the position of the  $\{CoG\}$  frame (while both of the two links are in contact with object) as  ${}^{(w)}\mathbf{r}_{contact}$ , the desired position of the  $\{CoG\}$  frame  ${}^{(w)}\mathbf{r}_{des}$  in first two sub-phases can be written as

$${}^{(w)}\mathbf{r}_{des} = {}^{(w)}\mathbf{r}_{contact} + {}^{(w)}\mathbf{r}_{offset} \quad (50)$$

On the other hand, the desired yaw angle  ${}^{(w)}\alpha_{z_{des}}$ , which is expressed in the  $\{CoG\}$  frame of the aerial robot, has already been set to its grasp phase value  ${}^{(w)}\alpha_{z_{grasp}}$ . As discussed in Section 3, the orientation of  $\{CoG\}$  is chosen to be identical to the baselink attached to the *Spinal* board. As the *Spinal* board is generally attached to the middle of the multilinks, as shown in Figure 5, either of the two links connecting by the center joint is the baselink. Therefore, the desired yaw angle of the  $\{CoG\}$  frame is the same as that of the baselink, indicating that the desired yaw angle of  $\{CoG\}$  frame is constant despite the transformation in the former sub-phase.

After the transformation, the aerial robot starts descending to the height at which it will grasp the object. Although turbulence from the floor and object gradually increases as

the aerial robot descends, the horizontal position and yaw angle do not drift much because they have converged in the first sub-phase. The altitude control is much more stable and robust than the horizontal positioning, because the collective thrust force directly affects this state, and the response speed is much higher than the horizontal position control that results from the attitude control.

**5.1.3. Approach to contact.** This sub-phase aims to achieve the two points of contact between the links at both sides of the center joint and object. Considering the large turbulence caused by the floor and the object, a feedforward acceleration control is adopted instead of the feedback position control. Two different methods are developed to obtain the desired acceleration control for a cylindrical and convex polygonal column, respectively.

**Cylinder** The desired acceleration can be obtained as the opposite of the approaching offset  ${}^{(w)}\mathbf{r}_{offset}$ :

$${}^{(w)}\ddot{\mathbf{r}}_{des} = a_{des} {}^{(w)}\hat{\mathbf{r}}_{P_{cj}P_o} \quad (51)$$

where  $a_{des}$  is the scalar value of the desired acceleration and  ${}^{(w)}\hat{\mathbf{r}}_{P_{cj}P_o}$  is the unit vector pointing from  $P_{cj}$  to  $P_o$ . As shown in Equation (26), there is a linear relationship between the acceleration and attitude if the yaw angle is constant and robot is almost level. Thus, the desired acceleration can be more easily achieved than the desired position. In addition, once the aerial robot contacts the object, the rolling motion of the duct on the surface is available, allowing another effective method to be used for relative position control between the object and aerial robot. Note that the altitude control is still based on the position control to maintain a constant height during this sub-phase and the third element of the desired acceleration is not used for the altitude control (theoretically, the third value should equal zero). Ideally, the acceleration control leads the two links (ducts) to contact the object simultaneously, although this is difficult to achieve in reality. In the case of one point contact, the rolling motion can compensate for the distance between the untouched link and the cylinder, as shown in Figure 17. The rolling motion requires firm contact at the pivot point and appropriate yaw control. Firm contact at the pivot point is satisfied by the constant acceleration by the aerial robot towards the object, which generates enough normal force at this point, whereas the yaw control is designed to generate the rotation in a constant direction:

$${}^{(w)}\alpha_{z_{des}} = {}^{(w)}\alpha_z + \Delta\alpha \quad (52)$$

where  ${}^{(w)}\alpha_z$  is the current yaw angle of the aerial robot,  $\Delta\alpha$  is a constant value to promote rotation, and the sign of  $\Delta\alpha$  is identical to the desired direction of rotation. Although a tactile sensor has generally been used to detect contact, it is difficult to apply the sensor all around the duct. Therefore, the relative distance between the duct and cylinder is calculated from their geometric features to determine whether contact has been made. The position of the duct center, i.e.,

the position of the corresponding rotor  $\mathbf{r}_{rotor_i}$ , can be easily obtained from the kinematics of the multilinks and the position of the  $\{CoG\}$  frame. Therefore, the gap between the duct and object can be calculated as follows:

$$d_{gap_i} = \| {}^{(w)}\mathbf{r}_{rotor_i} - {}^{(w)}\mathbf{r}_{object} \| - R_{duct} - R_{object} \quad (53)$$

where  $R_{duct}$  and  $R_{object}$  are the radius of duct and object, respectively, and  ${}^{(w)}\mathbf{r}_{object}$  denotes the center of the object. A minimum threshold is then applied to determine contact:

$$contact : d_{gap_i} < d_{thresh} \quad (54)$$

If valid contact is detected at the ducts on both sides of the center joint, the final approach is considered to be achieved. The center joint is then fixed at the grasp angle, indicating that the expected grasp form will be achieved in the later phase.

**Convex polygonal column** To grasp the convex polygonal column with the expected form, the desired angle  $\delta_{des}$  between the link and the corresponding surface (side) needs to be satisfied, in addition to the two points of contact. Thus, the desired acceleration and yaw angle design method for a cylinder cannot be applied, because the rotation of the yaw angle would fail to meet the  $\delta_{des}$  condition. This seems to be difficult to achieve the two points contact with desired  $\delta_{des}$  angle. Therefore, we take advantage of the polygon's geometric features to achieve the two points contact. First, we focus on the situation that only one of links on either side of center joint contacts the corresponding side of the polygon, and also assume that the angle  $\delta$  between this link and polygon side is equal to the desired value  $\delta_{des}$ . Then, a straightforward solution to achieve contact between the second link and corresponding side is to slide the multilinks along the direction of the first polygon side. Thus, the desired acceleration should coincide with this slide motion. Although this motion involves the slipping motion on the first polygon side, the desired acceleration is parallel to the first polygon side and a low normal force (and, thus, low fiction) can be assumed at the contact point. Consequently, there are two slide directions for each situation, as shown in Figure 18(a), and a weighted sum method can be used to combine these two elements according to the gap distance  $d_{gap}$ :

$${}^{(w)}\ddot{\mathbf{r}}_{des} = a_{des} {}^{(w)}\hat{\mathbf{b}} \quad (55)$$

$${}^{(w)}\mathbf{b} = \frac{d_{gap_1} {}^{(w)}\mathbf{n}_{\{C_1\},y} - d_{gap_2} {}^{(w)}\mathbf{n}_{\{C_2\},y}}{d_{gap_1} + d_{gap_2}} \quad (56)$$

$$d_{gap_i} = {}^{(w)}\mathbf{n}_{\{C_i\},x} \cdot ({}^{(w)}\mathbf{r}_{\{C_i\}} - {}^{(w)}\mathbf{r}_{rotor_i}) - R_{duct} \quad (57)$$

where  ${}^{(w)}\mathbf{r}_{\{C_i\}}$  is the origin position of the polygon side frame  $\{C_i\}$  with reference to the world frame  $\{W\}$ , which can be calculated from the object position  ${}^{(w)}\mathbf{r}_{object}$ . The unit vector  ${}^{(w)}\mathbf{n}_{\{C_i\},x}$  and  ${}^{(w)}\mathbf{n}_{\{C_i\},y}$  can be also easily obtained from the orientation matrix of the object  ${}^{(w)}R_{object}$ . This calculation is not performed when both links contact their

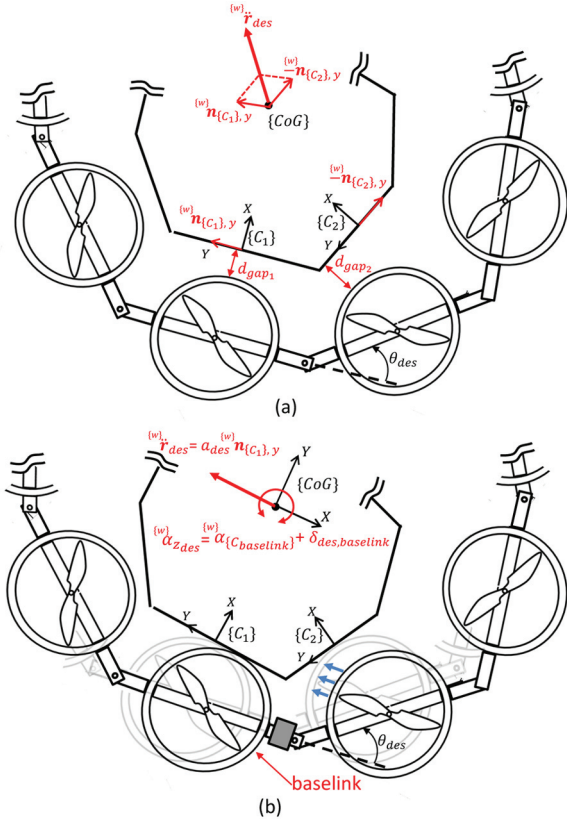


**Fig. 18.** The approach motion for contact in the case of a polygonal column: (a) the desired acceleration  $\{^W\vec{r}_{des}$  is the combination of the two vectors parallel to the direction of the  $y$ -axes of the corresponding contact frame  $\{C_i\}$ ; and (b) the slide motion can be achieved by the proposed acceleration  $\{^W\vec{r}_{des}$  parallel to the direction of the corresponding polygon side. The first-contacted link is assumed the baselink, which has same orientation with the  $\{CoG\}$  frame, allowing for calculation of the desired yaw angle of the aerial robot.

corresponding polygon sides; rather, the desired acceleration is set to zero. Thus, there is theoretically no normal force (and, thus, no friction) acting on the polygon sides during the motion sequence. The angle  $\delta_i$  between the  $i$ th link and the corresponding polygon side should, thus, converge to the desired value  $\delta_{i,des}$ . The orientation of the polygon side corresponding to the baselink can be obtained from the object orientation matrix  $\{^W\vec{R}_{object}$ , which then allows the yaw angle of the polygon side  $\alpha_{\{C_{baselink}\},z}$  to be obtained. Subsequently, the desired yaw angle of baselink and, thus, the  $\{CoG\}$  frame of aerial robot can be calculated as

$$\{^W\alpha_{z,des} = \{^W\alpha_{\{C_{baselink}\},z} + \delta_{baselink,des} \quad (58)$$

As discussed above, the normal force and friction are theoretically not generated during this approach motion and the yaw control is always feasible by the rolling motion as shown in Figure 18(b). A threshold is created to check the convergence of angle  $\delta$ ; this range can be set as the valid

range obtained from the grasp searching method in Section 4:

$$\text{convergence : } \underline{\delta}_{\text{baselink}} < \delta_{\text{baselink}} < \bar{\delta}_{\text{baselink}} \quad (59)$$

where  $\underline{\delta}_{\text{baselink}}$  and  $\bar{\delta}_{\text{baselink}}$  are the lower and upper bound of the valid range of  $\delta_{\text{baselink}}$ , respectively, corresponding to the grasping form searching result as shown in Figure 13. This convergence check only needs to be performed on the baselink, as if either  $\delta_1$  or  $\delta_2$  is convergent, the other is also theoretically convergent. Consequently, if valid contact is detected at both points of contact and angle  $\delta_{\text{baselink}}$  is convergent, the final approach has been achieved, allowing the robot to shift to the next grasp phase.

## 5.2. Grasp phase

Once the first two links properly contact the object, the other joints start to rotate to the desired grasping angle  $\theta_{i,des}$ . However, in reality, slight model errors could be introduced. For example, if the joint angle contains a small offset and the target objects is not an ideal cylindrical or convex polygonal column, the force-closure may not be achieved by the desired grasp form ( $\boldsymbol{\theta}_{des}$ ). Hence, a continuous small angle  $\Delta\theta_{grasp}$  is added at each joint until a certain load of the joint servo has been imposed, as shown in

$$\theta_{k+1,i} = \begin{cases} \theta_{k,i} + \Delta\theta_{grasp} & (\text{load}_i < \text{load}_{thresh}) \\ \theta_{k,i} & (\text{otherwise}) \end{cases} \quad (60)$$

Torque values are not used, as the torque generated by the joint servo is difficult to measure without employing a torque sensor inside the module. The compact servo module used in this proposed multilinked aerial robot is not suitable to contain a torque sensor. However, the servo load is assumed proportional to the torque value, and can be obtained from the current sensor inside the joint servo module or the servo feedback control output if no current sensor is available.

The link contact order is very important. If the end link contacts the object first, the robot may get stuck (Figure 14). Therefore, a grasping level order is introduced, where the center joint ( $i_{cj}$ ) is level 1, the two adjacent joints ( $i_{cj} + 1$  and  $i_{cj} - 1$ ) are level 2, and so on. Higher-level joints do not rotate until the load of all joints at the lower level exceeds the threshold.

It is also necessary to generate enough of a normal force (and, thus, friction) at the already contacted points to keep the relative static between the aerial robot and the object. Therefore, a constant acceleration  $\{^W\vec{r}_{des}$  pointing form the center joint  $P_{cj}$  to the object center  $P_O$  is applied. In other words, the horizontal translational motion control is still based on the acceleration control mode in this phase.

After all links properly contact the object, the joint servo load is adjusted according to the force-closure torque  $\tau_{des}$  selected from the searching method described in Section 4. However, the torque cannot be precisely measured and the

searching method in Section 4 assumes a general friction coefficient of 0.3. Nevertheless, the relative ratio among the elements of the torque vector is constant, regardless of a varying coefficient of friction and the object mass. Therefore, the desired load can be calculated as

$$load_{i_{des}} = load_{cons} \frac{\tau_{i_{des}}}{\min(\tau_{des})} \quad (61)$$

where  $\min(\tau_{des})$  denotes the minimum component in the desired joint torques  $\tau_{des}$  for force-closure. The constant value  $load_{cons}$  is assumed equal to  $load_{thresh}$  in Equation (60). The desired joint angle is adjusted with the small angle  $\Delta\theta_{load}$  to keep the load within a certain range around the desired value  $load_{i_{des}}$ :

$$\theta_{k+1,i} = \begin{cases} \theta_{k,i} + \Delta\theta_{load} & (load_i < load_{des,i} - \Delta load_{closure}) \\ \theta_{k,i} - \Delta\theta_{load} & (load_i > load_{des,i} + \Delta load_{closure}) \\ \theta_{k,i} & (\text{otherwise}) \end{cases} \quad (62)$$

### 5.3. Closure phase

Once the load of all the joint servos is within the valid range, the force-closure is considered achieved and the transportation motion can be performed. However, before lifting up, the robot model should be updated to calculate the correct feedback gains based on the transfer function

(11), including the total mass  $M$ , the rotor configuration matrix  $P$ , and the change of inertia tensor  ${}^{CoG}I$ .

## 6. Experiments

### 6.1. Robot platform

The quadrotor prototype shown in Figure 5 is used to perform the aerial transformation and the whole-body aerial manipulation; the entire system used to achieve the transformable flight is presented in Figure 19. The three-dimensional position  ${}^W\mathbf{r}$  and yaw angle  ${}^W\alpha_z$  are tracked by the external motion capture system, which can be regarded as the ground truth. The markers for motion capture are attached at the third link, which contains the *Spinal* board. Thus, this link is the baselink of which the frame orientation is identical to that of the CoG frame. The states measured by the motion capture are sent to the aerial robot via Wi-Fi and combined with other state information from the on-board IMU unit (e.g., acceleration  ${}^W\ddot{\mathbf{r}}$ ) to obtain overall knowledge about the ego-motion. Real-time updates regarding the LQI feedback gains are performed at about 20 Hz in the on-board high-level processor based on the current joint angles from the *Spinal* board. The position controller in the high-level processor runs at 40 Hz and sends the control output along with part of the LQI feedback gains to the *Spinal* board. Those values are

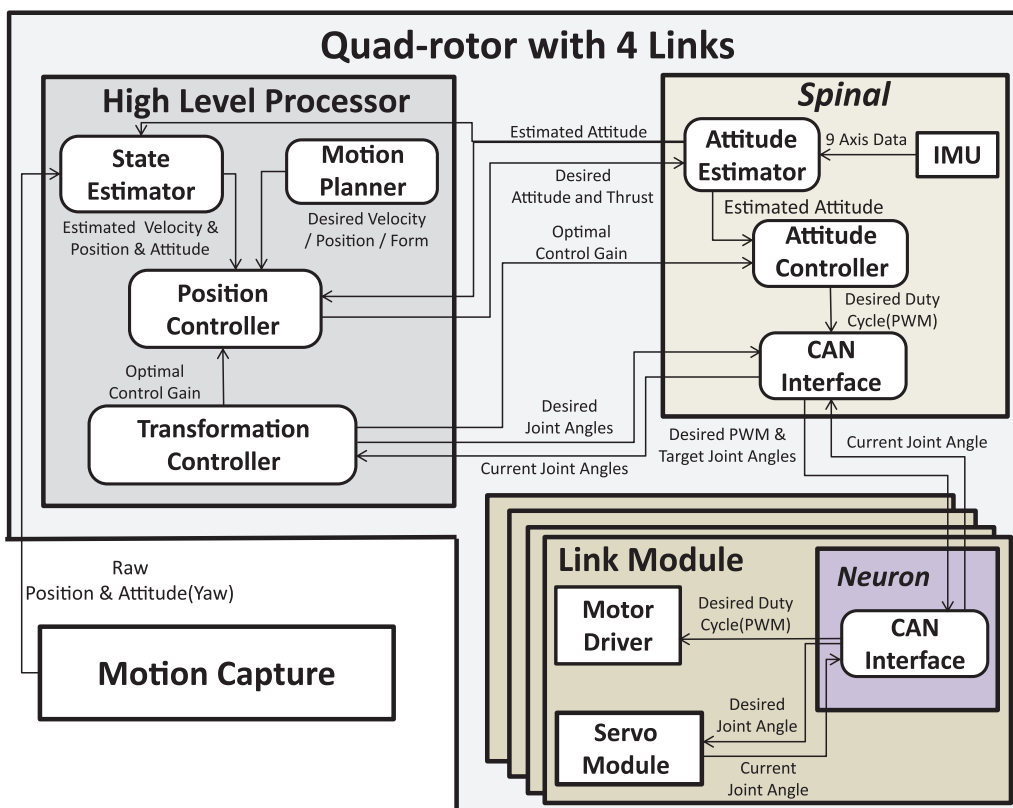
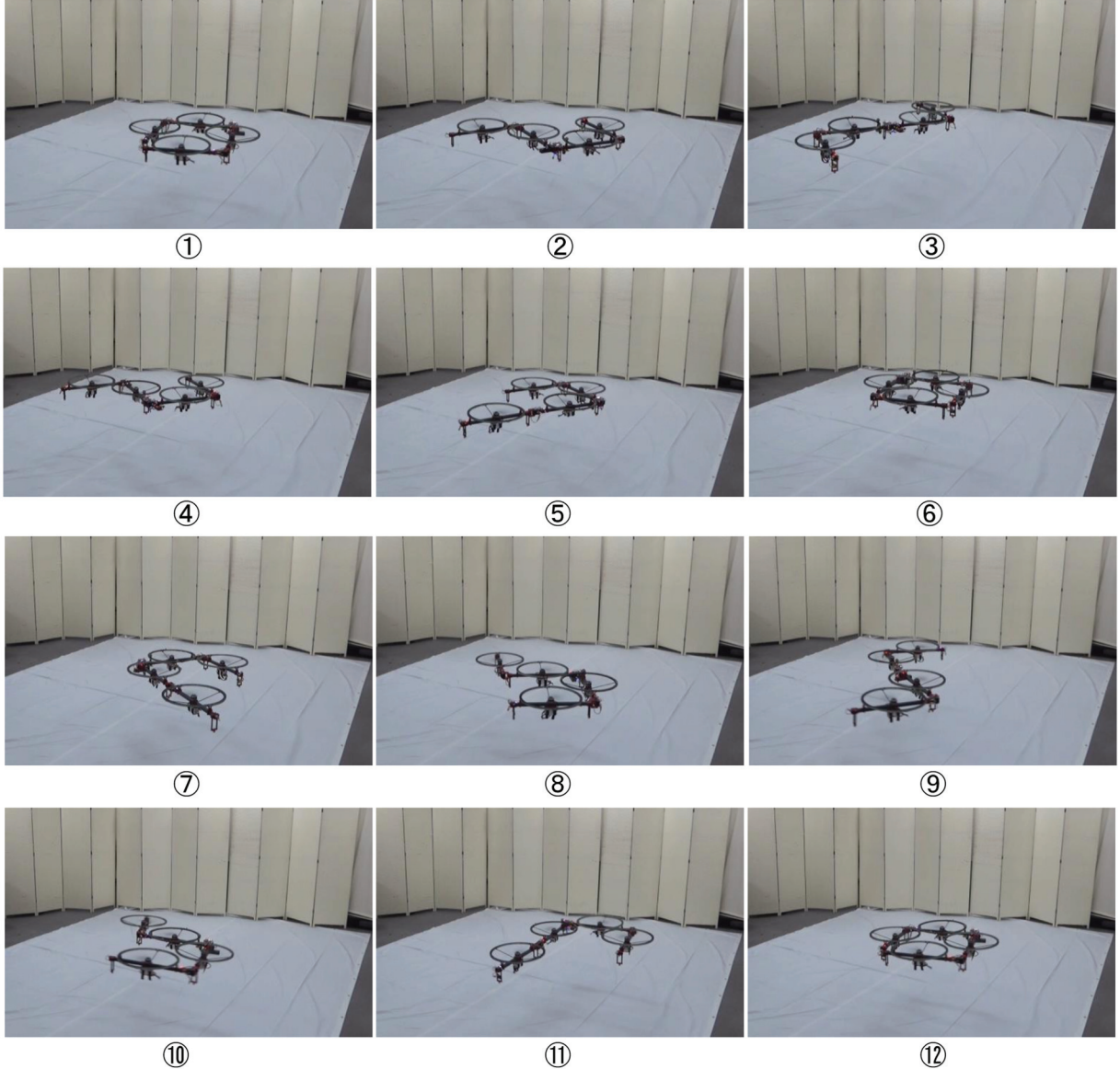


Fig. 19. Entire quadrotor system with four links based on the internal communication system.



**Fig. 20.** Photographs from the experimental trial of the large-scale aerial transformation. Videos of the experiments are available at <https://youtu.be/rXO7De03Knl>

used by the attitude controller, which runs at 500 Hz inside the *Spinal* board.

### 6.2. Aerial transformation

In our previous work (Zhao et al., 2016), the stable aerial transformation was operated within the full stabilizable range as discussed in Section 3. There, to avoid the singular forms during transformation, a fully stable path was generated based on RRT\* (Karaman and Frazzoli, 2010), which required significant processing resources, and resulted in poor real-time performance. Moreover, the transformation range was considerably limited, especially in the case of four links, leading to difficulty in aerial application. Therefore, we perform the relaxed hovering

solution to increase the valid range of aerial transformation, and thus the flight control method for semi-stabilizable forms is applied, as presented in Section 3.

The quadrotor prototype shown in Figure 5 is thus used to experiment on the large-scale aerial transformation, of which the transformation path is shown in Figure 21(a). The robot begins in the form  $\theta_1 = \frac{\pi}{2}$  rad,  $\theta_2 = \frac{\pi}{2}$  rad,  $\theta_3 = \frac{\pi}{2}$  rad, and finishes in the same form.

Representative images from the aerial transformation are given in Figure 20, and the change of the attitude  $\alpha$  (Euler angles) and translational error  $r_{err}$  are shown in Figure 21. The root mean square (RMS) of the translational error is [0.101, 0.119, 0.030], and the maximum errors are less than 0.25 m. The pitch and roll angles remain below 0.11 rad. These experimental results demonstrate the

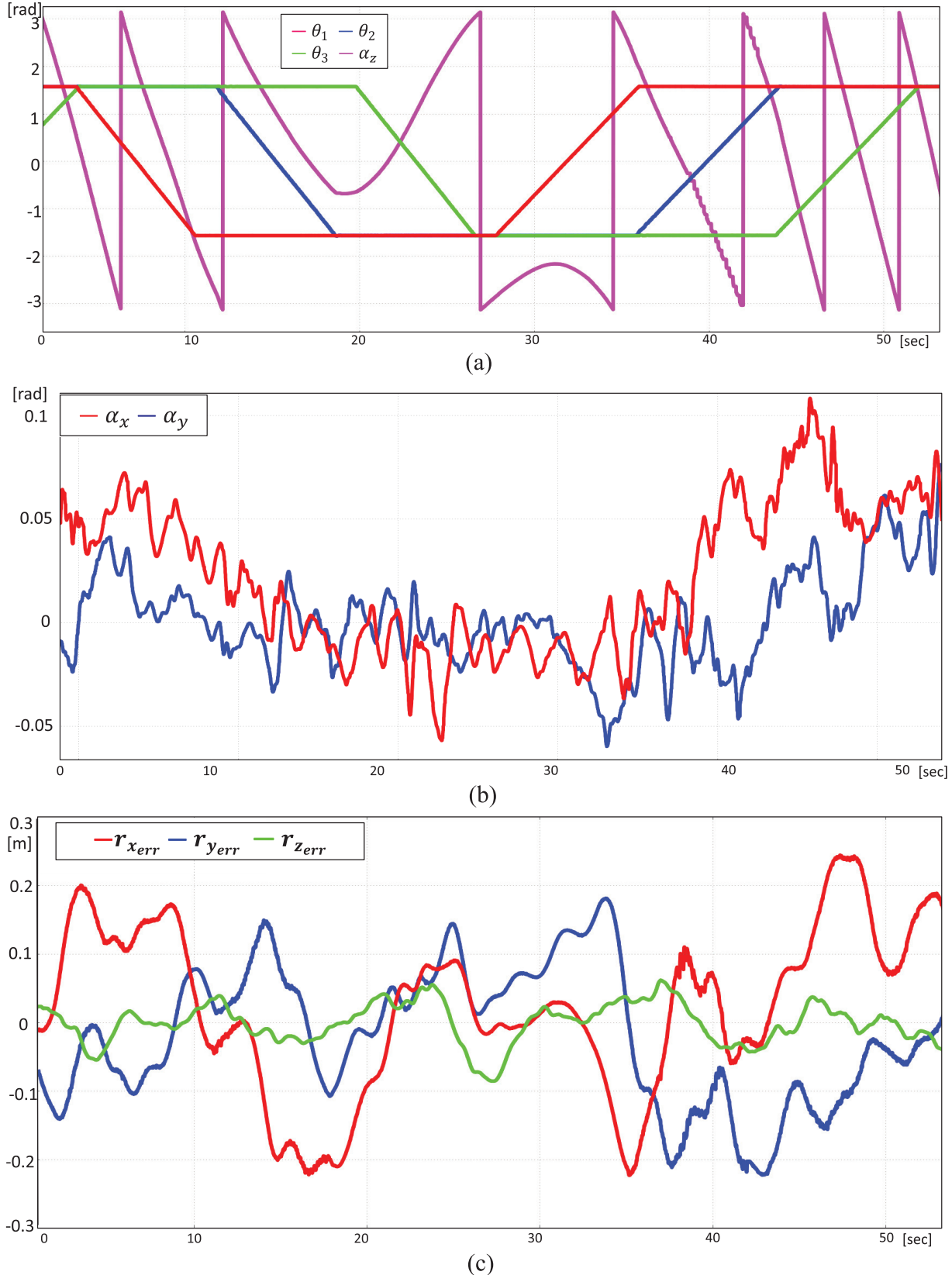


**Fig. 21.** From the large-scale aerial transformation experiment: (a) the path of the joint angles and the yaw angle of the aerial robot; (b) the change of the attitude in terms of pitching and rolling; and (c) the time series of the error regarding to the robot target position.

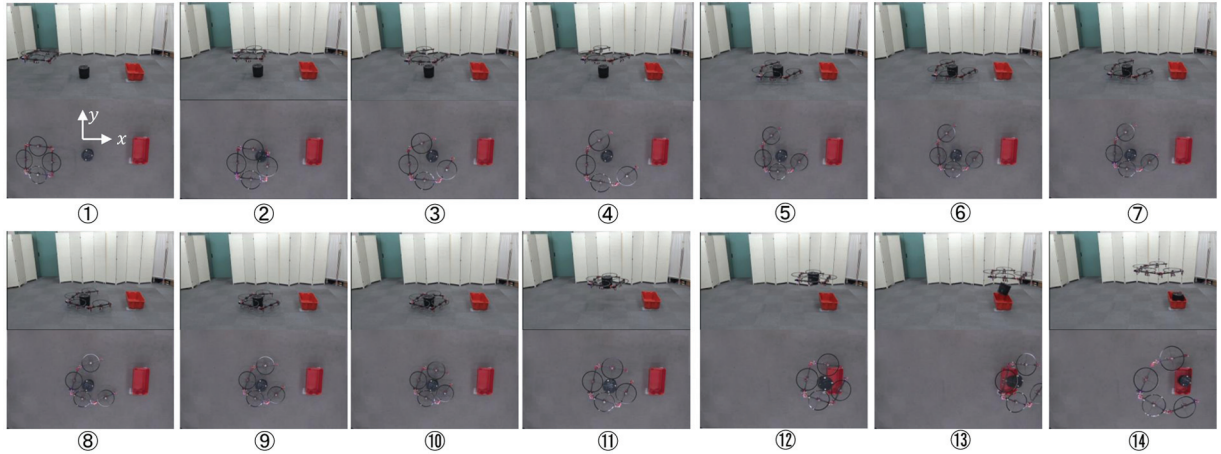


**Fig. 22.** Photographs of the experimental aerial manipulation procedure to transport a cylindrical-type object. Upper and lower images are captured from the side view and top view, respectively. The direction of the world frame  $\{W\}$  is shown in ①. Videos of the experiments performed are available at <https://youtu.be/rXO7De03KnI>

hovering stability in terms of the translational motion during the aerial transformation. As shown in Figure 21(a), the yaw angle of the CoG frame varies due to a lack of yaw control. The value of the thrust vector  $f_T$  at the hovering state is equal to the result of Equation (36). This value can be regarded as the nominal value and varies as the multi-links' form changes, resulting in a different moment around the  $z$ -axis of the CoG frame, which can be calculated as  $\sum c_i f_i$ . As shown in Figure 21(a), the yaw rotation does not accelerate and changes the rotational direction twice during the aerial transformation, as the sign of the total moment around the  $z$ -axis always changes.

Although, the robot passes through the singular form  $\theta_1 = -\frac{\pi}{2}$  rad,  $\theta_2 = 0$ ,  $\theta_3 = \frac{\pi}{2}$  rad in terms of  $R^3 \times SO(2)$ , during transformation, the translational stability are confirmed. The feasibility of the aerial transformation passing semi-stabilizable forms is therefore experimentally confirmed.

### 6.3. Whole-body aerial manipulation

Next, the experiment of picking up and carrying target objects to a case is performed to validate the proposed whole-body aerial manipulation method. The target cylindrical-type and box-type objects are built as specified in Figure 11. The sectional area of the cylinder and the box are  $\pi(\frac{0.25}{2})^2$  m<sup>2</sup> and 0.3<sup>2</sup> m<sup>2</sup>, respectively, and each weighs 1 kg. The three-dimensional positions of the objects are tracked by the motion capture system, indicating that object recognition and the real-time searching process of the optimized grasp form is not required. The desired grasp form  $\theta_{des}$  found from either Figure 12 or Figure 13 is applied by performing real-time flight control in the on-board processors according to the approach and grasp motion strategy described in Section 5. In addition to the phases as proposed in Figure 16 (i.e., approach phase, grasp phase, and

closure phase), we also demonstrate the motion of dropping object in this experiment.

As shown in Figures 22 and 25, the overall aerial manipulation process can be summarized as follows: ①~② moving to the approach position with the initial form and hovering above the object (the first sub-phase of the approach phase in Figure 16); ③~⑤ changing to the approach form and descending to surround the object (the second sub-phase of the approach phase); ⑥~⑧ approaching the object to achieve the first two points of contact (the thrust sub-phase of the approach phase); ⑨~⑩ grasping object until the force-closure is achieved (the grasp phase); ⑪~⑫ lifting off and carrying the object to the case (the closure phase); ⑬~⑭ moving over the case and then dropping object. To guarantee a high coefficient of friction to lift the object, a polishing sheet is stick to the edge of the propeller duct.

Although the stall torque of the servo motor used for joint module is known (3.1 Nm), it is difficult to identify the true coefficient of friction between the duct and the object's surface. Furthermore, the servo motor does not contain a current sensor and, thus, the torque control is not possible. However, as stated in Section 5, the relative ratio among the components in the desired torque  $\tau_{des}$  is important. Thus, we estimate the servo load based on the PID control regarding to the joint angle, which is considered proportional to the torque value. The load is then normalized within a range of  $[-1, 1]$ , where the sign of the load indicates the direction of the torque. The load threshold  $load_{thresh}$  used to detect grasping in Equation (60), and the minimum load  $load_{cons}$  used for force-closure in Equation (61), are both set to 0.2. It is confirmed possible to lift the target objects with those values.

#### 6.3.1. Grasping and carrying the cylindrical-type object.

The motion shown in images ⑥~⑧ in Figure 22

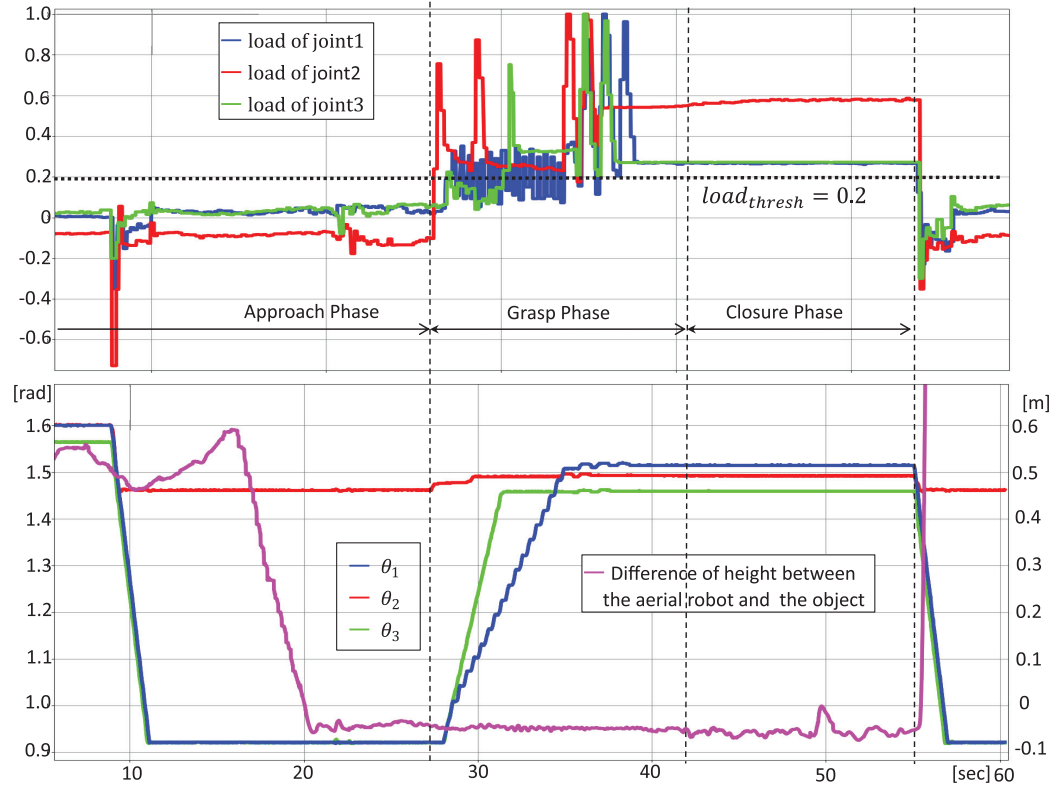


**Fig. 23.** Top: the normalized load of each joint. Bottom: the angle of each joint, and the difference of height between aerial robot and object.

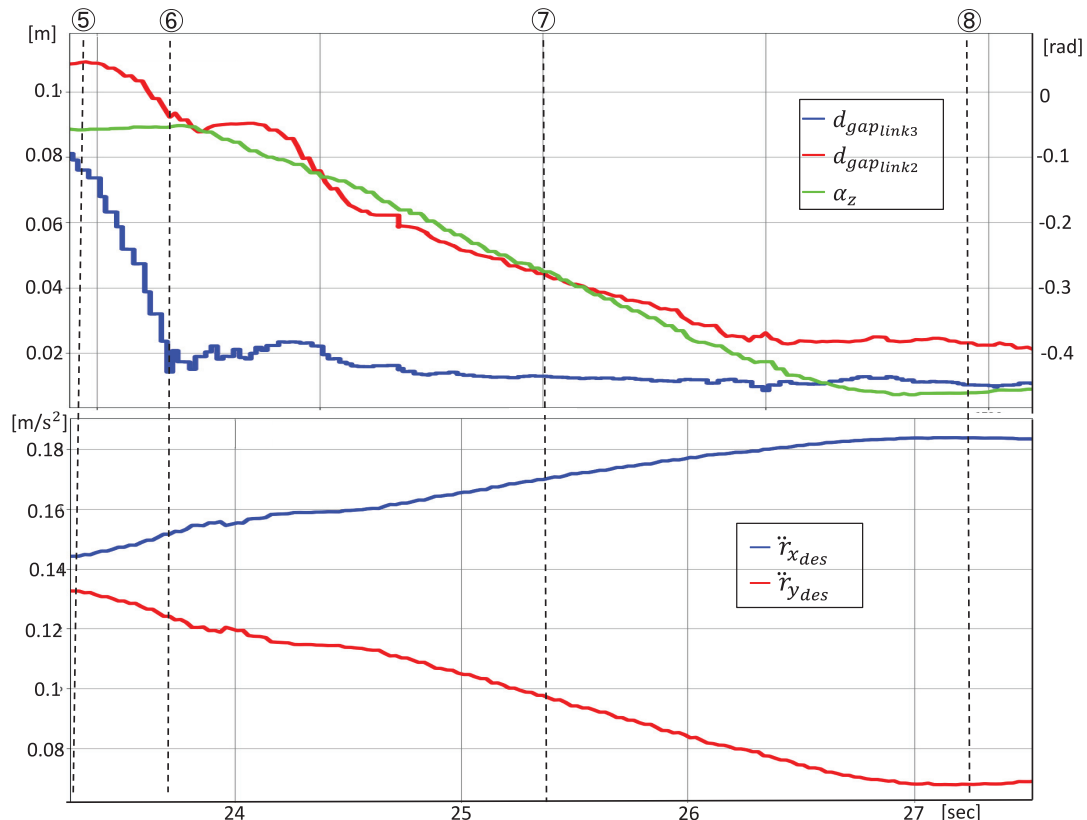


**Fig. 24.** Experimental results detailing with the third sub-phase in the approach phase. Top: the change of the distance between object and each link,  $d_{gap_{link_i}}$ , and the yaw angle of aerial robot,  $\{^W\}\alpha_z$ . Bottom: the change of the desired acceleration of the aerial robot,  $\{^W\}\dot{r}_{des}$ .

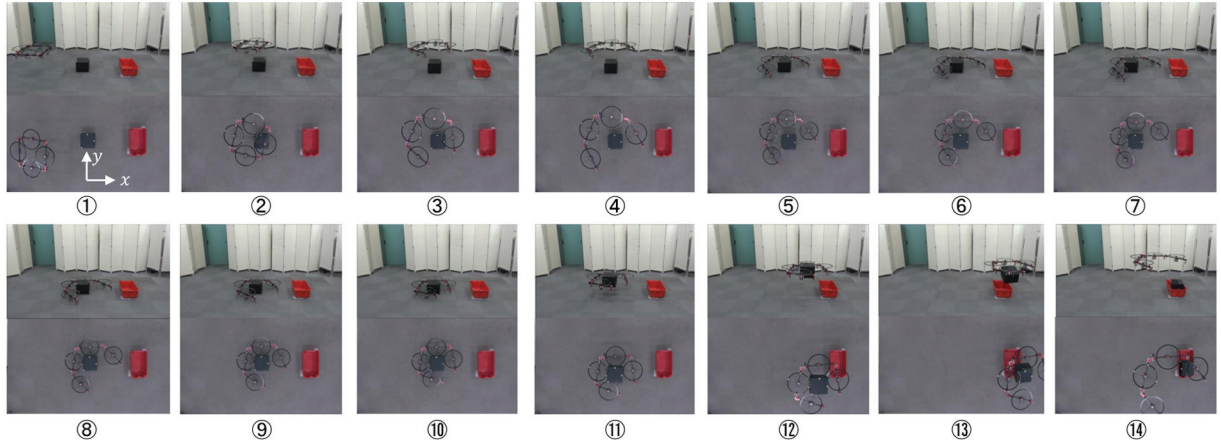


**Fig. 25.** Photographs of the experimental aerial manipulation procedure to transport a box-type object. Upper and lower images are captured from the side view and top view, respectively. The direction of the world frame  $\{W\}$  is shown in ①. Videos of the experiments performed are available at <https://youtu.be/rXO7De03KnI>

demonstrates the rolling motion along the cylinder surface as shown in Figure 17 in the third sub-phase of the approach phase. As shown in Figure 24, the third link ( $link_3$ ) contacts the object first. However, the contact distance  $d_{gap}$  (Equation (53)) does not converge to zero under the contacted situation, owing to the model error (e.g., the shape of object is not a perfect cylinder) along with the sensing noise from motion capture and the joint angles. Thus, the contact distance threshold  $d_{thresh}$  (Equation (54)) is set to 0.03 m to guarantee a large enough margin for contact detection. During the rolling motion, the desired acceleration value changes with the rotation of the yaw angle  ${}^{(w)}\alpha_z$  as shown Figure 24, because the direction of desired acceleration must remain parallel to the direction of  $r_{P_{ej}P_o}$  as shown in Figure 17.

After the two points are confirmed to have made contact (e.g., ⑧ in Figure 22), the robot shifts to the grasp phase. Here, the center and level 1 joint is the second joint  $j_2$ . Theoretically, the center joint should not change its angle during the grasp phase, because the links on both sides of this joint are already in contact with the object. However, the center joint  $j_2$  does adjust its angle, as shown in Figure 23. We consider this is due to the threshold used to check contact (Equation (54)), which allows the small distance (e.g., <0.03 m) between the object and the duct. Nevertheless, the angle change at the center joint is relatively small, and the level 2 joints are then adjusted as described in Equation (60). Once contact is confirmed between each link and the object, load adjustment is performed based on the desired grasp torque  $\tau_{des}$  according to Equation (62) to complete the force-closure. As shown in Figure 23, the estimated load at each joint is very chattering at initial grasp phase, likely because of the slight vibration from the robot attitude control while the object is static with respect to the floor. This vibration could lead to the slight slipping at each contact point, making the joint load

unstable. However, once the force-closure is confirmed, the object is lifted off the floor, and becomes stable.

The grasp form obtained during closure phase is  $\boldsymbol{\theta} = [1.51, 1.49, 1.46]$ , which is nearly within the valid range of the searching result presented in Figure 12. Theoretically, the first and third joint angles should be equivalent. The discrepancy reveals the sensing and model errors, as discussed above. On the other hand, the height difference between the aerial robot and the grasped object is relatively constant, demonstrating the effectiveness of the grasp planning method to achieve the force-closure. The small variation of this relative height difference (e.g., 50 s as shown in Figure 23) is likely caused by the sudden tilt of the aerial robot changing the target positions.

After releasing the motion, the aerial robot quickly ascends, because the weight of aerial robot dropped rapidly and the integral term of the LQI cannot update to the new weight configuration rapidly enough. Although the expected value could be simultaneously subtracted while dropping the object, the integral term is allowed to slowly decrease and the robot altitude is back to the correct value after approximately 10 s.

**6.3.2. Grasping and carrying the box-type object.** As shown in Figure 25, the procedure to approach, grasp, and carry away a box-type object is similar to that of the cylindrical-type object. Thus, similar phenomena, such as the variance of height difference between the aerial robot and the object during the closure phase, are seen. Some differences are observed, including a sliding motion in the third sub-phase of the approach phase, as shown in Figure 27. Here, the distance  $d_{gap_{link2}}$  between  $link_2$  and the corresponding object side decreases gradually, whereas  $link_3$  is already in contact with the object. As the desired acceleration is always parallel to the polygon side corresponding to  $link_3$ , there is less friction at this contact point, and thus the

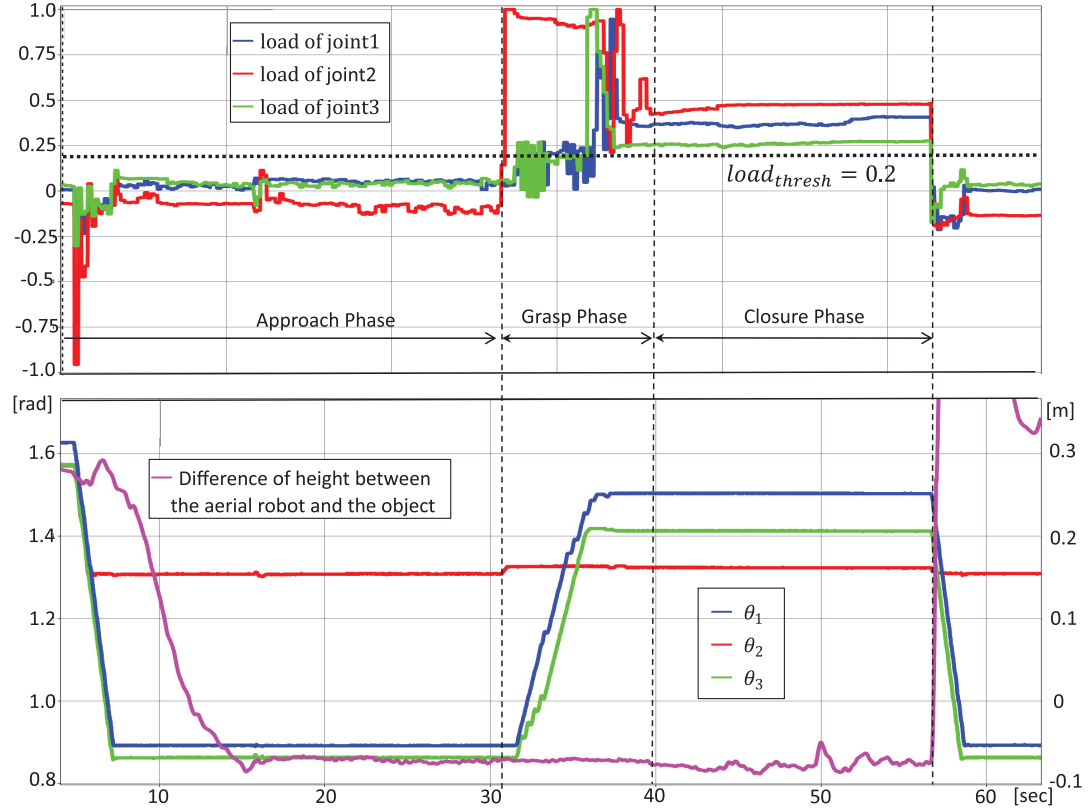


**Fig. 26.** Top: the normalized load of each joint. Bottom: the angle of each joint, and the difference of height between aerial robot and object.

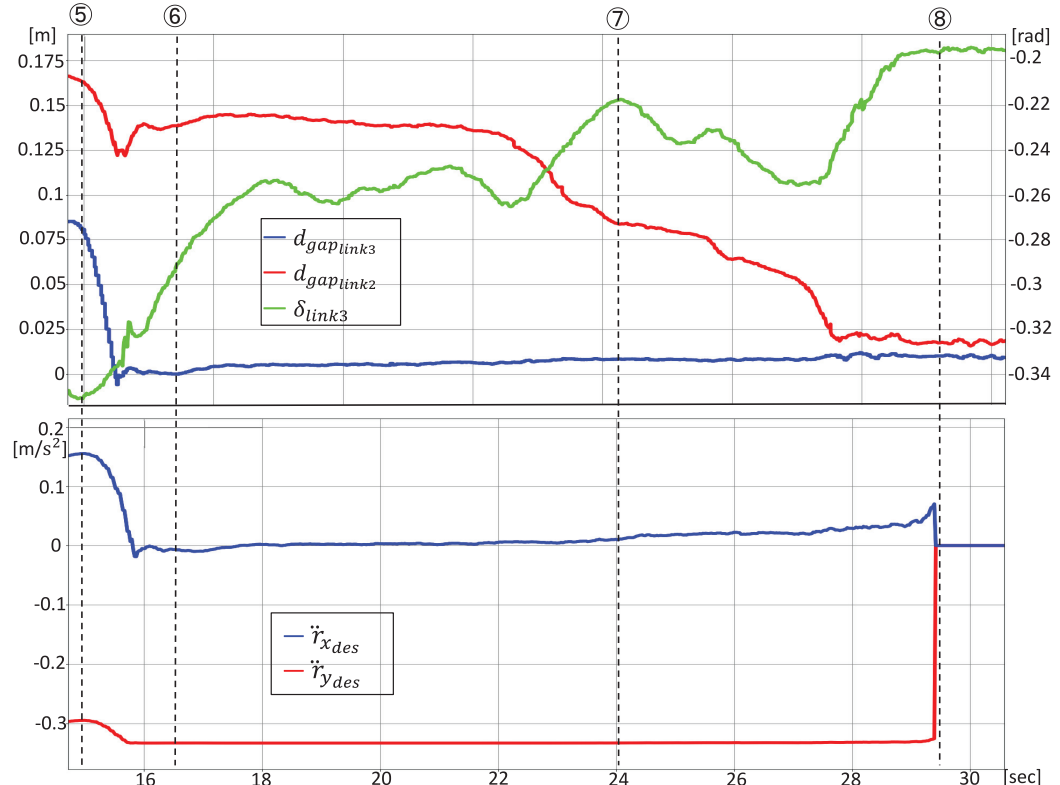


**Fig. 27.** Experimental results detailing the third sub-phase in the approach phase. Top: the change of the distance between object and each link,  $d_{gap_{link_i}}$ , along with the angle between  $link_3$  (the baselink) and the corresponding polygon surface,  $\delta_{links}$ . Bottom: the change of the desired acceleration of the aerial robot,  $\{W\}r_{des}$ .

aerial robot does not get stuck. Meanwhile, the desired angle  $\delta_{link3}$  also converges into the valid range  $[-0.225, -0.137796]$ .

The grasp form reached during the closure phase is  $\theta = [1.50, 1.32, 1.41]$ , which is nearly within the calculated valid range shown in Figure 13. The slight difference seen in this trial is also likely associated with the sensing and model errors.

## 7. Conclusions and future work

The aerial transformation and whole-body aerial manipulation using a multilinked multirotor with an internal communication system has been studied. A modular link structure and reliable internal communication system to connect the links was first developed. The quadrotor prototype composed of four links has also been demonstrated. A flight control method for the stable hovering of the multirotor under variable forms based on an LQI optimal servomechanism control system has then been introduced and a relaxed hover solution focusing only on the translational stability without yaw control for certain singular forms, defined as semi-stabilizable forms, was proposed. A methodology of whole-body aerial manipulation has then been introduced from two aspects: (i) an optimized grasp-form searching method based on the kinematics and statics of multilinks along with a force-closure condition; and (ii) an aerial approach and grasp motion strategy to achieve the expected grasp form found by the searching method. The experimental results confirmed the feasibility of the large-scale aerial transformation and then the aerial manipulation picking up and carrying cylindrical-type and box-type objects.

Future work will focus on enhancing flight stability during the aerial transformation by applying the robust control based on the dynamics of the multilinks. Applying this robust control can also improve the whole-body aerial manipulation while operating the approach and grasp motions. We are also pursuing the development of the object recognition by on-board sensors to address the online form searching issue to grasp objects of unknown shape, along with the reactive motion planning based on sensor feedback during the approach and grasp phases.

## References

- Anzai T, Zhao M, Chen X, et al. (2017) Multilinked multirotor with internal communication system for multiple objects transportation based on form optimization method. In: *2017 IEEE/RSJ International Conference on Intelligent Robots and Systems (IROS)*, pp. 5977–5984.
- Backus SB, Odhner LU and Dollar AM (2014) Design of hands for aerial manipulation: Actuator number and routing for grasping and perching. In: *2014 IEEE/RSJ International Conference on Intelligent Robots and Systems*, pp. 34–40.
- Bouabdallah S and Siegwart R (2007) Full control of a quadrotor. In: *IEEE/RSJ International Conference on Intelligent Robots and Systems, 2007 (IROS 2007)*, pp. 153–158.
- Cho S and Shim DH (2017) Development of a vision-enabled aerial manipulator using a parallel robot. *Transactions of the Japan Society for Aeronautical and Space Sciences, Aerospace Technology Japan* 15: a27–a36.
- Doitsidis L, Weiss S, Renzaglia A, Kosmatopoulos E, Siegwart R and Scaramuzza D (2012) Optimal surveillance coverage for teams of micro aerial vehicles in GPS-denied environments using onboard vision. *Autonomous Robots* 33(1–2): 173–188.
- Ferreau H, Kirches C, Potschka A, Bock H and Diehl M (2014) qpOASES: A parametric active-set algorithm for quadratic programming. *Mathematical Programming Computation* 6(4): 327–363.
- Gawel A, Kamel M, Novkovic T, et al. (2017) Aerial picking and delivery of magnetic objects with mavs. In: *2017 IEEE International Conference on Robotics and Automation (ICRA)*, pp. 5746–5752.
- ISO (1993) Road vehicles - interchange of digital information - controller area network (CAN) for high-speed communication. ISO 11898.
- Karaman S and Frazzoli E (2010) Incremental sampling-based algorithms for optimal motion planning. In: *Proceedings of Robotics: Science and Systems*, Zaragoza, Spain.
- Kawasaki K, Motegi Y, Zhao M, Okada K and Inaba M (2015) Dual connected bi-copter with new wall trace locomotion feasibility that can fly at arbitrary tilt angle. In: *2015 IEEE/RSJ International Conference on Intelligent Robots and Systems (IROS)*, pp. 524–531.
- Kojima K, Karasawa T, Kozuki T, et al. (2015) Development of life-sized high-power humanoid robot JAXON for real-world use. In: *15th IEEE-RAS International Conference on Humanoid Robots (Humanoids 2015)*, Seoul, South Korea, 3–5 November 2015, pp. 838–843.
- Kumar V and Michael N (2012) Opportunities and challenges with autonomous micro aerial vehicles. *The International Journal of Robotics Research* 31(11): 1279–1291.
- Lindsey Q, Mellinger D and Kumar V (2012) Construction with quadrotor teams. *Autonomous Robots* 33(3): 323–336.
- Lippiello V, Cacace J, Santamaría-Navarro A, et al. (2016) Hybrid visual servoing with hierarchical task composition for aerial manipulation. *IEEE Robotics and Automation Letters* 1(1): 259–266.
- Mahony R, Kumar V and Corke P (2012) Multirotor aerial vehicles: Modeling, estimation, and control of quadrotor. *IEEE Robotics Automation Magazine* 19(3): 20–32.
- Mellinger D, Lindsey Q, Shomin M and Kumar V (2011) Design, modeling, estimation and control for aerial grasping and manipulation. In: *2011 IEEE/RSJ International Conference on Intelligent Robots and Systems*, pp. 2668–2673.
- Mellinger D, Shomin M, Michael N and Kumar V (2013) *Cooperative Grasping and Transport Using Multiple Quadrotors*. Berlin: Springer, pp. 545–558.
- Michael N, Mellinger D, Lindsey Q and Kumar V (2010) The grasp multiple micro-UAV testbed. *IEEE Robotics Automation Magazine* 17(3): 56–65.
- Michael N, Shen S, Mohta K, et al. (2012) Collaborative mapping of an earthquake-damaged building via ground and aerial robots. *Journal of Field Robotics* 29: 832–841.
- Mueller MW and D'Andrea R (2016) Relaxed hover solutions for multicopters: Application to algorithmic redundancy and novel vehicles. *The International Journal of Robotics Research* 35(8): 873–889.

- Oung R and D'Andrea R (2014) The distributed flight array: Design, implementation, and analysis of a modular vertical take-off and landing vehicle. *The International Journal of Robotics Research* 33(3): 375–400.
- Oung R, Ramezani A and D'Andrea R (2009) Feasibility of a distributed flight array. In: *Proceedings of the 48h IEEE Conference on Decision and Control (CDC) held jointly with 2009 28th Chinese Control Conference*, pp. 3038–3044.
- Pak PS, Suzuki Y and Fujii K (1974) Synthesis of multivariable linear optimal servo-system incorporating integral-type controllers. *Transactions of the Society of Instrument and Control Engineers* 10(1): 1–5.
- Pounds PEI, Bersak DR and Dollar AM (2011) Grasping from the air: Hovering capture and load stability. In: *2011 IEEE International Conference on Robotics and Automation (ICRA)*, pp. 2491–2498.
- Seo J, Kim S and Kumar V (2012) Planar, bimanual, whole-arm grasping. In: *2012 IEEE International Conference on Robotics and Automation (ICRA)*, pp. 3271–3277.
- Tsai LW (1999) *Robot Analysis and Design: The Mechanics of Serial and Parallel Manipulators*. 1st ed. New York: John Wiley & Sons, Inc.
- Urata J, Nakanishi Y, Okada K and Inaba M (2010) Design of high torque and high speed leg module for high power humanoid. In: *2010 IEEE/RSJ International Conference on Intelligent Robots and Systems*, pp. 4497–4502.
- Watanabe T, Harada K, Yoshikawa T and Jiang Z (2006) Towards whole arm manipulation by contact state transition. In: *2006 IEEE/RSJ International Conference on Intelligent Robots and Systems*, pp. 5682–5687.
- Young PC and Willems JC (1972) An approach to the linear multivariable servomechanism problem. *International Journal of Control* 15(5): 961–979.
- Zhao M, Kawasaki K, Chen X, Noda S, Okada K and Inaba M (2017) Whole-body aerial manipulation by transformable multirotor with two-dimensional multilinks. In: *2017 IEEE International Conference on Robotics and Automation (ICRA)*, pp. 5175–5182.
- Zhao M, Kawasaki K, Okada K and Inaba M (2016) Transformable multirotor with two-dimensional multilinks: modeling, control, and motion planning for aerial transformation. *Advanced Robotics* 30(13): 825–845.